Covalency in Lanthanides. An X-ray Absorption Spectroscopy and Density Functional Theory Study of $LnCl_6^{x-}$ (x = 3, 2)

Matthias W. Löble,[†] Jason M. Keith,[†,‡] Alison B. Altman,[∥] S. Chantal E. Stieber,[†] Enrique R. Batista,*,[†] Kevin S. Boland,[†] Steven D. Conradson,[†] David L. Clark,[†] Juan Lezama Pacheco,[⊥] Stosh A. Kozimor,*,[†] Richard L. Martin,*,[†] Stefan G. Minasian,[§] Angela C. Olson,[†] Brian L. Scott,[†] David K. Shuh,[§] Tolek Tyliszczak,[§] Marianne P. Wilkerson,[†] and Ralph A. Zehnder[#]

[†]Los Alamos National Laboratory, Los Alamos, New Mexico 87545, United States
[‡]Colgate University, Hamilton, New York 13346, United States
[§]Lawrence Berkeley National Laboratory, Berkeley, California 94720, United States
[∥]University of California, Berkeley, California 94720, United States
[⊥]Stanford University, Stanford, California 94305, United States
[#]Angelo State University, San Angelo, Texas 76909, United States

Ⓢ *Supporting Information*

ABSTRACT: Covalency in Ln−Cl bonds of O_h-$LnCl_6^{x-}$ (x = 3 for Ln = Ce[III], Nd[III], Sm[III], Eu[III], Gd[III]; x = 2 for Ln = Ce[IV]) anions has been investigated, primarily using Cl K-edge X-ray absorption spectroscopy (XAS) and time-dependent density functional theory (TDDFT); however, Ce L$_{3,2}$-edge and M$_{5,4}$-edge XAS were also used to characterize $CeCl_6^{x-}$ (x = 2, 3). The M$_{5,4}$-edge XAS spectra were modeled using configuration interaction calculations. The results were evaluated as a function of (1) the lanthanide (Ln) metal identity, which was varied across the series from Ce to Gd, and (2) the Ln oxidation state (when practical, i.e., formally Ce[III] and Ce[IV]). Pronounced mixing between the Cl 3p- and Ln 5d-orbitals ($t_{2g}*$ and e_g*) was observed. Experimental results indicated that Ln 5d-orbital

mixing decreased when moving across the lanthanide series. In contrast, oxidizing Ce[III] to Ce[IV] had little effect on Cl 3p and Ce 5d-orbital mixing. For $LnCl_6^{3-}$ (formally Ln[III]), the 4f-orbitals participated only marginally in covalent bonding, which was consistent with historical descriptions. Surprisingly, there was a marked increase in Cl 3p- and Ce[IV] 4f-orbital mixing ($t_{1u}*$ + $t_{2u}*$) in $CeCl_6^{2-}$. This unexpected 4f- and 5d-orbital participation in covalent bonding is presented in the context of recent studies on both tetravalent transition metal and actinide hexahalides, MCl_6^{2-} (M = Ti, Zr, Hf, U).
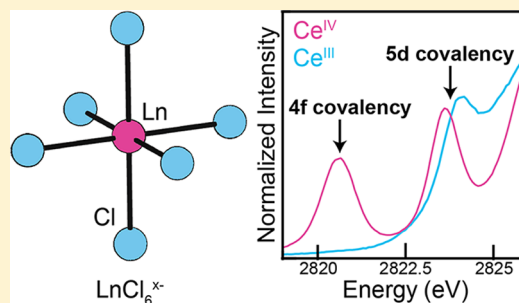
■ INTRODUCTION

Despite recent advances, it remains of considerable interest to better define the roles that f- and d-orbitals play in chemical bonding in lanthanides and actinides.[1−5] Advent of new theory and spectroscopic techniques has provided insight into f- and d-orbital mixing in actinide metal−ligand bonds.[6−8] However, bonding for the 4f-lanthanide (Ln) elements is often described as primarily ionic,[2−4,6−12] largely because previous calculations indicated that the 4f-orbitals do not extend significantly beyond the core orbitals.[13−18] The viewpoint that lanthanide−ligand interactions are best described using ionic bonding models finds support in the literature from many reactivity studies and physical measurements. Most notably, optical spectroscopy suggests that the 4f-orbitals are core-like and only weakly influenced by ligand fields.[19−21] However, a number of 4f-element compounds have been isolated where covalency in bonding may be important,[22−38] and a growing number of studies suggested that the 5d-orbitals should be considered when evaluating lanthanide−ligand bonding.[1−5,18,39−42] As the

use of rare earth elements is increasing in many industrial processes[43]—e.g. in catalysis, energy production, medicine, lighting materials, high-performance alloys, magnets, and areas relevant to national security—it is becoming more important to understand these anomalies and advance descriptions of lanthanide electronic structure and covalent bonding.

Perhaps the most versatile and direct approach to evaluate covalency utilizes a combination of ligand K-edge X-ray absorption spectroscopy (XAS)[6−8,44−56] and time-dependent density functional theory (TDDFT).[6−8,50,57−60] Using orbital descriptions, the spectroscopic approach involves quantifying the intensity of bound-state transitions between ligand 1s-orbitals and virtual (unoccupied) orbitals. Because the hole is localized on the ligand, the dominant contribution to the dipole matrix element governing the intensity can be associated with the component of ligand p-character in the final state.

Scheme 1. Cartoon Depicting Electronic Excitations in a Typical Ligand K-Edge XAS Experiment
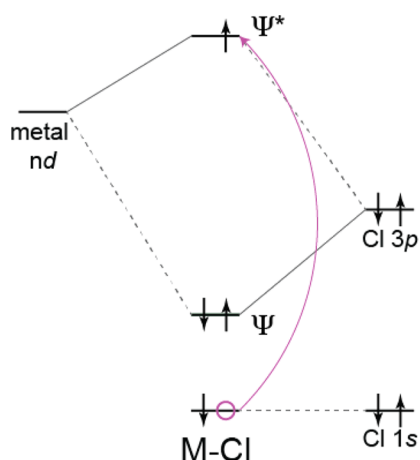
Transitions into an unoccupied orbital of principally metal character (Scheme 1) imply a component of ligand p-character in that orbital. Measuring the experimental intensities then provides an estimate of the associated metal−ligand orbital mixing. Strictly speaking, the observed intensities reflect atomic orbital mixing in the unoccupied orbitals. However, in the simple orbital models used to interpret bonding, any atomic orbital mixing present in an unoccupied orbital reflects mixing in the occupied orbital, due to the orthogonality constraints on the two orbitals that contain ligand p-character. Hence, as we define orbital mixing as a synonym for covalency (in the sense of Heitler and London[1]), ligand K-edge XAS provides a direct estimate of metal−ligand covalency.[48]

To provide guidance for the interpretation of the experimental work, the TDDFT computational approach involves modeling the XAS spectra using a linear response theory calculation, where the energy and oscillator strength of excitations from the core levels to virtual orbitals can be determined. Combined, these experimental (XAS) and theoretical (TDDFT) methods operate cooperatively and have been implemented to evaluate orbital mixing in many transition metal systems.[6−8,44−66]

Herein, we have exploited the recent successes of ligand K-edge XAS and TDDFT in evaluating covalency in actinides[6−8,60,66−68] to provide the first in a series of Ln−Cl covalency studies. Orbital mixing in the Ln−Cl bond was evaluated in a series of highly symmetric O_h-$LnCl_6^{x−}$ (Ln = Ce, Nd, Sm, Eu, Gd, x = 3; Ln = Ce, x = 2) anions. In contrast to many traditional assumptions, comparing our spectroscopic and theoretical results from $LnCl_6^{3−}$ (formally Ln^{III}) revealed that the 5d-orbitals were involved in covalent Ln−Cl bonding with the 4f-orbitals playing a minimal role. For the case of $CeCl_6^{2−}$, where the unusual Ce^{IV} oxidation state could be investigated, we found evidence for both 4f- and 5d-orbital participation in bonding. Overall, the results are presented in the context of recent studies on analogous transition metal and actinide compounds, $MCl_6^{2−}$ (M = Ti, Zr, Hf, U).[7]

RESULTS AND DISCUSSION

$LnCl_6^{x−}$ Synthesis. The Cl K-edge, Ce $L_{3,2}$-edge, and Ce $M_{5,4}$-edge XAS techniques were used to analyze a series of lanthanide hexachloride salts containing organic cations of the general formula Z_3LnCl_6 (Ln = Nd^{III}, Sm^{III}, Eu^{III}, Gd^{III} and Z = NEt_4; Ln = Ce^{III} and Z = PPh_4) and $(NEt_4)_2CeCl_6$. These analytes—referred to hereafter as $LnCl_6^{x−}$ (x = 3, 2)—were carefully selected because they contain highly symmetric O_h-$LnCl_6^{x−}$ anions, which facilitated evaluating Ln−Cl bonding owing to the separability of the 4f- and 5d-orbitals in an octahedral ligand field. The $LnCl_6^{x−}$ analytes were attractive because they can be prepared in large quantities and in high purity. All of the hexachlorides were made using slight modifications of previously published synthetic procedures.[69−73] For instance, the $LnCl_6^{3−}$ (formally Ln^{III}) compounds were isolated from reactions between anhydrous $LnCl_3$ and 3 equiv of either NEt_4Cl or PPh_4Cl, while $Ce(SO_4)_2·xH_2O$ was used to make $CeCl_6^{2−}$ (formally Ce^{IV}). All of the products were characterized by single-crystal X-ray diffraction (XRD). A representative thermal ellipsoid plot for $CeCl_6^{2−}$ has been provided in Figure 1. Crystallographic
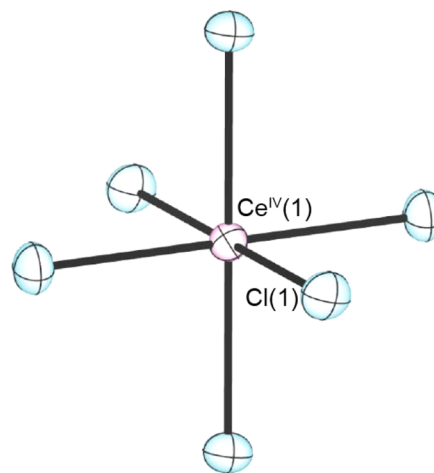
Figure 1. Thermal ellipsoid plot of $(NEt_4)_2CeCl_6$. Thermal ellipsoids are drawn with 50% probability. The NEt_4^{1+} countercations are omitted.

analysis of $(NEt_4)_2CeCl_6$ (formally Ce^{IV}) was consistent with the previous report.[69] Although the Z_3LnCl_6 (formally Ln^{III}) structures had not been reported, the Ln−Cl bond distances and Cl−Ln−Cl angles observed in this study were consistent with other octahedral $LnCl_6^{3−}$ salts.[69−73] In all the $LnCl_6^{3−}$ structures, the solid state analyses revealed that the large non-coordinating cations guarded against bridging Cl interactions and ensured that the M−Cl bond was probed discretely during Cl K-edge XAS measurements. Most notably, especially in regard to the XAS and DFT experiments, the Ln−Cl distances were equivalent once the metal ionic radii were considered (Table 1), suggesting that the Ln−Cl bond was best described using an ionic bonding model. Moreover, there was no indication from the structural metrics that the amount of Ln−Cl orbital mixing varied appreciably. As will be discussed, the XAS and DFT results provided unambiguous evidence for profound changes in orbital mixing between $CeCl_6^{2−}$ and the $LnCl_6^{3−}$ anions.

Ce $L_{3,2}$-Edge XAS. In light of recent electronic structure studies that have addressed the possibility of intermediate valency for Ce compounds with formal oxidation states of IV,[5,24,42,74−93] the $CeCl_6^{3−}$ and $CeCl_6^{2−}$ compounds were characterized at the Ce $L_{3,2}$-edges. The Ce L_3-edge extended X-ray absorption fine structure (EXAFS) data were initially used to confirm that synchrotron experiments were conducted on pure $CeCl_6^{3−}$ and $CeCl_6^{2−}$ analytes. Measurements were made

Table 1. Average Bond Distances (Å) for the Z_3LnCl_6 (Ln = Nd, Sm, Eu, Gd and Z = NEt$_4$; Ln = Ce and Z = PPh$_4$) and $(NEt_4)_2CeCl_6$ Compounds, Compared with the DFT-Calculated Values[a]

	expt			DFT	
compound	Ln–Cl	SD[a]	Ln–Cl minus Ln ionic radii[a]	Ln–Cl mean	SD[a]
$CeCl_6^{3-}$	2.77	0.02	1.76	2.6715	0.0001
$PrCl_6^{3-}$	–	–	–	2.860	0.008
$NdCl_6^{3-}$	2.74	0.02	1.75	2.8451	–
$PmCl_6^{3-}$	–	–	–	2.8286	–
$SmCl_6^{3-}$	2.71	0.01	1.75	2.820	0.004
$EuCl_6^{3-}$	2.70	0.01	1.75	2.817	0.021
$GdCl_6^{3-}$	2.69	0.02	1.75	2.8273	–
$CeCl_6^{2-}$	2.599(1)	–	1.73	2.8843	0.00013

[a]Standard deviation from the mean. [a]Ionic radii-corrected Ln–Cl distances, using Shannon ionic radii.[165]
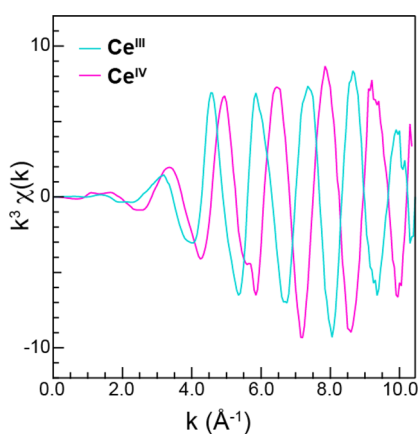
Figure 2. Ce L_3-edge EXAFS function $k^3\chi(k)$ for $CeCl_6^{3-}$ (aqua trace) and $CeCl_6^{2-}$ (pink trace) collected at 100 K. See Supporting Information for the details of the EXAFS fits.

at both 100 and 6 K. In Figure 2, the $k^3\chi(k)$ data (100 K) for both $CeCl_6^{3-}$ and $CeCl_6^{2-}$ are shown. This comparison highlighted the phase shift and change in frequency for the EXAFS oscillations between the two analytes, which was attributed to differences in Ce–Cl bond distances. The data were modeled by allowing the bond length distribution variance, σ^2 (Debye–Waller factor), and the bond length (R) to converge to reasonable values, while the number of neighboring atoms in the inner scattering shell was fixed at six Cl atoms based on the crystallographic data (Figure 3). The proximity of the Ce L_2-edge (~6164 eV) constrained meaningful EXAFS data to less than ~11k. As a result, scattering pathways beyond the first coordination shell (including multiple scattering pathways, e.g., Cl–Ce–Cl) were not included. However, satisfactory models of the EXAFS data (100 K) were obtained and the Ce–Cl bond distances were determined to be 2.62(2) Å ($\sigma^2 = 0.0034 \pm 0.0008$) for $CeCl_6^{2-}$ and 2.79(2) Å ($\sigma^2 = 0.0027 \pm 0.0005$) for $CeCl_6^{3-}$. These distances were consistent with the single-crystal XRD measurements, which showed a crystallographically unique Ce^{IV}–Cl bond distance of 2.599(1) Å in $CeCl_6^{2-}$ and an average 2.77 Å (standard deviation of 0.02 Å at 1σ) distance in $CeCl_6^{3-}$. Although not shown in Figure 3, analyses of EXAFS data from $CeCl_6^{3-}$ and $CeCl_6^{2-}$ collected at 6 K were in good agreement with the 100 K measurements discussed above.
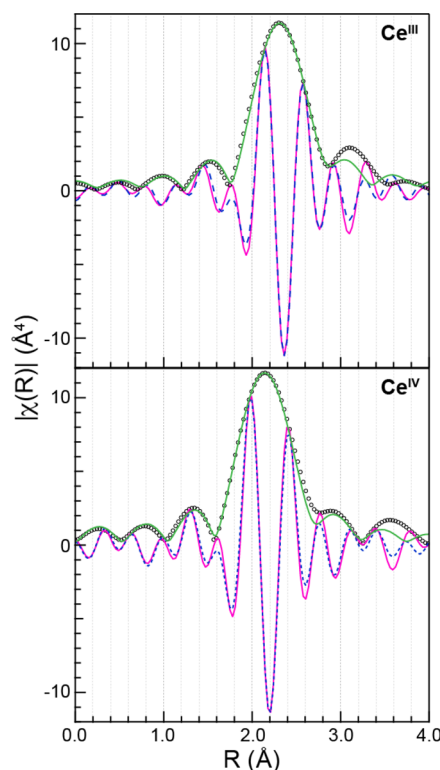
Figure 3. Fourier transforms of the Ce L_3-edge EXAFS function $k^3\chi(k)$ for $CeCl_6^{3-}$ (O, top) and $CeCl_6^{2-}$ (O, bottom) collected at 100 K. Fits to the data are represented by the green and dashed blue traces.

In Figure 4, the background-subtracted and normalized Ce $L_{3,2}$-edge XAS spectra from $CeCl_6^{3-}$ and $CeCl_6^{2-}$ are provided.
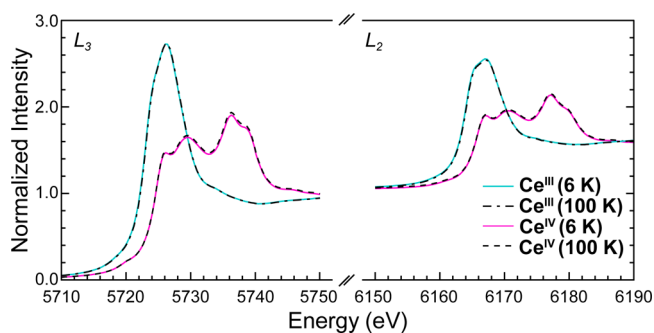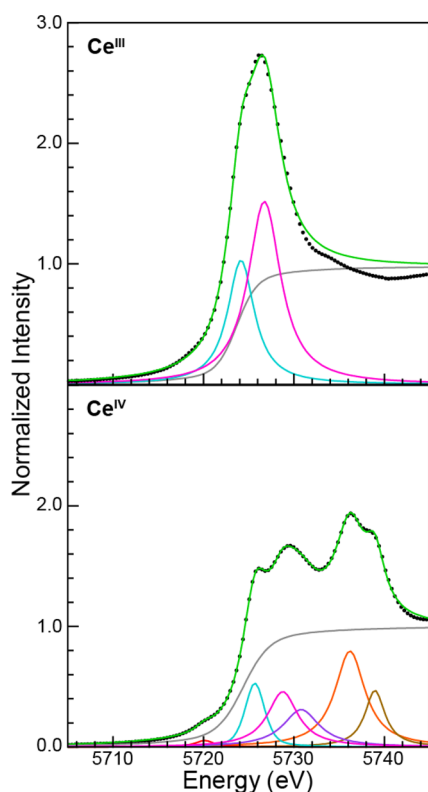

Figure 4. Ce $L_{3,2}$-edge XAS spectra of $CeCl_6^{3-}$ (pink trace) and $CeCl_6^{2-}$ (aqua trace) at 6 K. The dashed traces show the $CeCl_6^{3-}$ and $CeCl_6^{2-}$ spectra obtained at 100 K.

From the perspective of the free ion, the edge features in these spectra originated from electric-dipole allowed transitions from Ce 2p-orbitals to unoccupied states that contain Ce 5d-character, e.g. in $CeCl_6^{3-}$ there were $2p^64f^15d^0 \rightarrow 2p^54f^15d^1$ transitions. These final states were split into two primary L_3- and L_2-edges, owing to spin–orbit coupling of the $2p^5$ core–hole. For $CeCl_6^{3-}$, varying the temperature from 100 to 6 K had no detectable effect on the pre-edge peak intensities, as the high-temperature spectra were superimposable on the low-temperature measurements. Superficially, the $L_{3,2}$-edge peak positions from $CeCl_6^{3-}$ were similar to those of previously analyzed Ce^{III} compounds and were characterized by pronounced absorption edges with inflection points of 5723.1 (L_3-edge) and 6164.1 eV (L_2-edge).[75–93] The $L_{3,2}$-edge peak

intensity ratio was determined to be 0.47(2) using a graphical approach based on the integration of the second-derivative spectrum, and defined as $A_3/(A_3 + A_2)$. Here, A_3 and A_2 represent the total areas under the second derivative of the L_3- and L_2-edge peaks, respectively. The $CeCl_6^{3-}$ spectrum was interesting in comparison to the spectra of other Ce^{III} compounds in that the $L_{3,2}$-edge peaks clearly consisted of two dominant features. Consistently, curve-fitting analysis suggested that the spectrum (100 K; between 5710 and 5730 eV) was best modeled by two Lorentzian functions separated by 2.6 eV, which was in agreement with the second derivative of the data.

As observed for $CeCl_6^{3-}$, the $CeCl_6^{2-}$ $L_{3,2}$-edge XAS data also showed no dependence on temperature. Both the 6 and 100 K $L_{3,2}$-edge XAS data from $CeCl_6^{2-}$ were best described by double white line features and were consistent with previous analyses of Ce^{IV} compounds, i.e., $Ce(C_8H_8)_2$,[83,86] CeO_2,[24,74−76,80,90,91,85] $Ce(SO_4)_2·4H_2O$,[75,76] and CeF_4.[78,80] The inflection points for the rising edges (L_3 = 5724.7 eV and L_2 = 6165.7 eV) were approximately 1.5 eV higher in energy than those observed for $CeCl_6^{3-}$. The 0.52(2) $L_{3,2}$-edge peak intensity ratio was larger than the $CeCl_6^{3-}$ ratio of 0.47(2). Curve-fitting analyses indicated that the $CeCl_6^{2-}$ L_3-edge XAS spectrum (100 K; Figure 5) was modeled best using six Lorentzian functions. This model provided the best fit with the fewest functions and was in good agreement with analysis of the second derivative of the data. There was a low-energy pre-edge feature (red trace, 5720.1 eV) at the onset of a white line doublet, which has been attributed previously in other Ce^{IV} spectra to quadrupole-forbidden 2p→4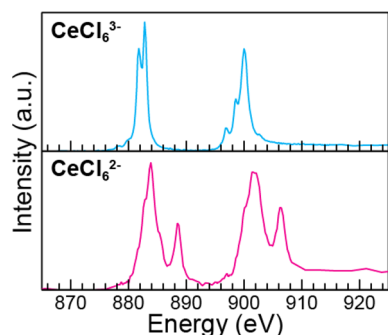f transitions.[85,90,91] The white line doublet was defined by a set of intermediate- and high-energy peaks. The intermediate features were modeled with three Lorentzian functions, (5725.7, 5728.8, and 5730.8 eV; aqua, pink, purple traces), while the high-energy peaks were modeled using a pair of Lorentzian functions (5736.2 and 5739.0 eV; orange and brown traces). In this sense, the $CeCl_6^{2-}$ Ce $L_{3,2}$-edge XAS spectra were unique in comparison to data previously reported from Ce^{IV} compounds,[24,74−93] whose white line doublets often had less fine structure and were typically defined by only three functions.
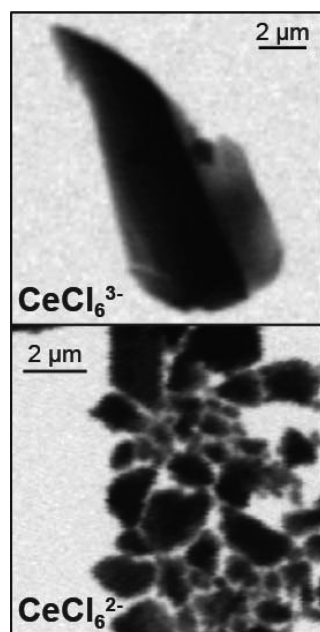
For comparison with previously reported spectra, Ce L_3-edge peak intensity ratios for the intermediate- (P_I) and high-energy (P_H) features were determined using $P_H/(P_H + P_I)$, where P_I and P_H represented the total areas under the intermediate- (aqua, pink, and purple traces, 5720−5734 eV) and high-energy (orange and brown traces, 5734−5742 eV) functions. We note that curve-fitting metrics from models with the step function at low energy (as shown in Figure 5) gave similar intensity ratios to models where the step function was pushed above 5745 eV (similar to that reported by Bianconi and co-workers[75,76]). The 0.51(5) intensity ratio determined for $CeCl_6^{2-}$ was reminiscent of the ratio determined for CeO_2 (0.54)[75,76] and smaller than that reported for $Ce(C_8H_8)_2$ (0.89).[86] Based on recent studies, this peak intensity ratio could be interpreted in different ways, either as a $4f^1$ contribution to a multiconfigurational ground-state or as resulting from final state effects. These concepts have ignited new theoretical discussions and it is surprising that with only simple Cl ligands, $CeCl_6^{2-}$ may exhibit unusual electronic properties, like CeO_2 and $Ce(C_8H_8)_2$. Clearly, understanding electronic structure and bonding in $CeCl_6^{2-}$ will benefit from additional X-ray absorption measurements. Hence, we compare subsequently the $CeCl_6^{2-}$ Ce $L_{3,2}$-edge XAS data with Ce $M_{5,4}$-edge and Cl K-edge XAS results, while future work is focused on fully characterizing $CeCl_6^{2-}$ bonding using other approaches.

Ce $M_{5,4}$-Edge XAS. Because exciting electrons from 3d-core orbitals at the $M_{5,4}$-edges directly probes the valence 4f-orbitals, Ce $M_{5,4}$-edge XAS provides an opportunity to uniquely evaluate f-electron occupancy and electronic structure in the $CeCl_6^{x-}$ compounds.[94−103] The intense multiplet structure associated with these $M_{5,4}$-edge XAS spectra—as well as the $M_{5,4}$-edge intensity ratios—has been previously used to characterize Ce orbital occupancies[104] in many lanthanide oxides,[105] metals,[106] and other lanthanide materials.[107−110] From the perspective of the free ion, features in Ce $M_{5,4}$-edge XAS spectra originate from electric-dipole-allowed transitions from Ce 3d-orbitals to unoccupied states that contain some degree of 4f-character, e.g., the $3d^{10}4f^n5d^0 \rightarrow 3d^94f^{n+1}5d^0$ transition.[94−103] For Ce, these final states are further split into two primary M_5- and M_4-edges owing to spin−orbit coupling of the $3d^9$ core−hole.

The background-subtracted $M_{5,4}$-edge XAS spectra obtained from samples of $CeCl_6^{3-}$ and $CeCl_6^{2-}$ in transmission mode using a scanning transmission X-ray microscope (STXM) are provided in Figure 6 from the particles shown in Figure 7. For $CeCl_6^{3-}$, the Ce M_5-edge (near 880 eV) and the Ce M_4-edge (~910 eV) portions of the spectra were best described as having a large peak that was further split into a series of less intense features. This "sawtooth" splitting pattern was consistent with previous $M_{5,4}$-edge spectra obtained from other Ce^{III} compounds.[106] The fine structure observed for $CeCl_6^{3-}$ also closely resembles the multiplet structure calculated for $3d^94f^2$ final states by Thole and co-workers[106]

Figure 5. Ce L_3-edge XAS experimental data (●) obtained from $CeCl_6^{3-}$ (top) and $CeCl_6^{2-}$ (bottom) at 100 K. The Lorentzian functions (red, aqua, pink, purple, orange, brown traces) and arctangent (gray) functions used to generate the deconvoluted spectra (green trace) are included.

Figure 6. Ce $M_{5,4}$-edge XAS spectra of $CeCl_6^{3-}$ (top, blue trace) and $CeCl_6^{2-}$ (bottom, pink trace).

Figure 7. X-ray contrast images taken above and bellow the Ce M5-edges showing the particles of $CeCl_6^{3-}$ (top) and $CeCl_6^{2-}$ (bottom) used to obtain the Ce $M_{5,4}$-edge XAS spectra shown in Figure 6.

and by modeling using the CTM4XAS program (*vide infra*).[111−113]

From an atomic perspective, assuming a single final-state configuration $(3d^94f^1)$ for formally tetravalent Ce $(4f^0)$ compounds, we would expect one peak for the Ce M_5- and M_4-edges (similar to La^{3+}).[106,111−113] However, the Ce $M_{5,4}$-edge XAS spectrum from $CeCl_6^{2-}$ was composed of intense main peaks at 883.7 and 901.6, respectively, and additional weaker satellite features at 888.6 and 906.4 eV. In this regard the Ce $M_{5,4}$-edge XAS of $CeCl_6^{2-}$ was reminiscent of experimental measurements from other formally Ce^{IV} compounds, such as CeO_2.[93] The M_5- and M_4-edges were split by 17.8 eV for $CeCl_6^{2-}$ and 17.2 eV for $CeCl_6^{3-}$, owing to differences in spin−orbit coupling with the $3d_{5/2}$ and $3d_{3/2}$ core−holes. Peak areas were determined using a graphical approach based on integration of the second derivatives.[114] The $M_{5,4}$-edge total intensity ratios—defined as $A_5/(A_5 + A_4)$, where A_5 and A_4 were the total areas under all M_5- or M_4-edge peaks[98,115]—increased from 0.48(2) to 0.50(3) on moving from $CeCl_6^{2-}$ to $CeCl_6^{3-}$. Given that $M_{5,4}$-edge intensity ratios have been reported to be dependent on the 4f-electron occupancy,[81,105−108] the increase in the magnitude of these

values was consistent with the anticipated decrease in the number for 4f-electrons for $CeCl_6^{2-}$ relative to $CeCl_6^{3-}$. However, we note that branching ratio values were equivalent once the error associated with the measurement was considered.

The presence of well-separated peaks in the $M_{5,4}$-edge spectra of $CeCl_6^{2-}$ (formally Ce^{IV}) provided an opportunity to evaluate the Ce 4f-orbital contribution to Ce−Cl bonding. In many ways, the spectrum from $CeCl_6^{2-}$ was reminiscent of many other formally Ce^{IV} compounds. Most notable was the similarity between two parameters used previously by Kaindl and co-workers to evaluate f-orbital occupancy, namely (1) the satellite-to-main peak intensity ratio and (2) the energy splitting between the main peaks and the satellite features. For instance, the satellite-to-main peak intensity ratio was measured to be 0.39(2) for $CeCl_6^{2-}$. Likewise, energy splittings between the main peaks and satellite features were 4.9 eV for $CeCl_6^{2-}$. Taken together, the Ce $M_{5,4}$-edge XAS spectra and measurements made at the Ce $L_{3,2}$-edge XAS (discussed above) provided a unified picture, suggesting that the Ce 4f-orbital contribution to bonding in $CeCl_6^{2-}$ closely resembled that of other Ce^{IV} compounds.

To unravel the origin of the satellite in the Ce^{IV} spectra, configuration interaction (CI) calculations for the $M_{5,4}$-edge XAS spectra from $CeCl_6^{x-}$ ($x = 2, 3$) were conducted using a semiempirical approach with the program CTM4XAS by de Groot.[111−113] This model allowed for core−hole-induced charge transfer, exchange, and multipole interactions to be included in the calculation.[116] To prepare the reader for what follows, we note that the calculations were performed in the atomic orbital representation. For $CeCl_6^{3-}$ (formally Ce^{III}), calculations employing a transition from single $3d^{10}4f^1$ initial state to the multiplet states associated with a $3d^94f^2$ final state configuration suitably modeled the experimental spectra (Figure 8). In agreement with previously reported Ce^{III} $M_{5,4}$-edge XAS calculations, Ce^{III} bond covalency could be accounted for by decreasing the 4f−4f Slater−Condon Coulomb repulsion parameter.[117−119] In our calculations this 4f−4f repulsion parameter and the 3d spin−orbit coupling (SOC) parameter were reduced to 79% and 98% of the atomic Hartree−Fock values, respectively. A Gaussian broadening of 0.25 eV was applied to account for instrumental broadening and Lorentzian broadenings of 0.2 and 0.4 eV were applied to the M_5- and M_4-edges, respectively. We note that in the absence of a reduction of the 3d SOC the M_5- and M_4-edge separation was overestimated and in the absence of a reduction of the 4f−4f Slater−Condon Coulomb repulsion the fine structure of the M_5-edge was not well modeled. We interpret the good correlation between the CI calculation and the experimental data as suggesting that the XAS spectra were dominated by interactions of the core 3d hole with 4f states, and contributions from the ligand field were of less concern.

For $CeCl_6^{2-}$ (formally Ce^{IV}), the experimental spectra could not be modeled successfully by considering only a $3d^{10}4f^0$ initial state and the final states (multiplets) associated with a $3d^94f^1$ configuration. In contrast to the Ce^{III} data described above, this result implied that for $CeCl_6^{2-}$ the atomic (ionic) limit was not appropriate. In an attempt to better understand the origins for the rich $CeCl_6^{2-}$ $M_{5,4}$-edge XAS spectral features—especially the higher energy satellites—charge-transfer effects were considered.[120−122] In the charge transfer model, the initial state was described by two possible configurations ($3d^{10}4f^0$ and $3d^{10}\underline{L}4f^1$) and the final state by the two configurations $3d^94f^1$
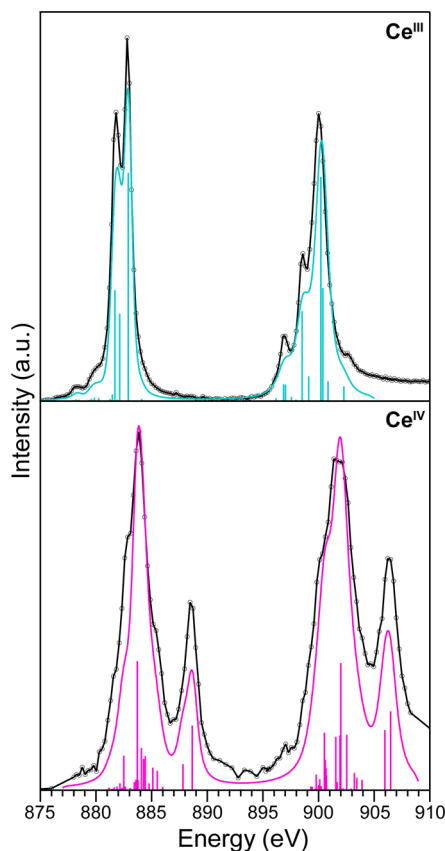
Figure 8. Comparison of the experimental (O, black traces) and the configuration interaction calculation (pink and aqua traces) for the Ce $M_{5,4}$-edge XAS spectra from $CeCl_6^{x-}$ ($x = 3$, top; $x = 2$, bottom). The bars represent the energy and oscillator strength for the calculated transitions.

Figure 9. UV−vis spectrum from $(NEt_4)_2CeCl_6$ (1.2×10^{-5} M) dissolved in acetonitrile. Data were acquired using a quartz cell (path length = 1 cm).

and $3d^9\underline{L}4f^2$, where $\underline{L}$ designates a hole in the ligand orbital. Each configuration was defined by 4f−4f Coulomb repulsion, 4f−3d$_{core}$ Coulomb repulsion, SOC, and Coulomb exchange parameters. Four additional parameters were defined to describe the relative energies and interactions of these states. These adjustable parameters consisted of the charge transfer energy (ΔE_{gs}) between the two ground-state configurations and the effective hopping integral (T_{gs}) connecting the two,

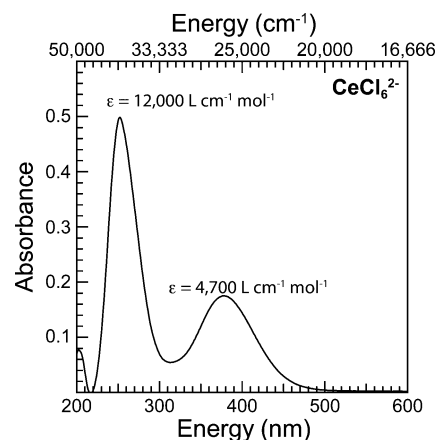$$\Delta E_{gs} = E(3d^{10}\underline{L}4f^1) - E(3d^{10}4f^0)$$

$$T_{gs} = \left\langle (3d^{10}\underline{L}4f^1)|H|(3d^{10}4f^0) \right\rangle$$

and two analogous parameters for the core−hole excited state (ΔE_{fs} and T_{fs}),

$$\Delta E_{fs} = E(3d^9\underline{L}4f^2) - E(3d^94f^1)$$

$$T_{fs} = \left\langle (3d^9\underline{L}4f^2)|H|(3d^94f^1) \right\rangle$$

To confine this parameter space, we chose to impose the constraint that the hopping integrals in the initial and final states should be identical. In addition, because the difference in energy between the two roots corresponding to the initial state CI corresponds to the LMCT band in the model, the experimental UV−vis spectrum was obtained (Figure 9). The $CeCl_6^{2-}$ UV−vis spectrum consists of two intense peaks, one at 3.3 eV ($\varepsilon = 4\,700$ L cm^{-1} mol^{-1}) and an additional peak at 4.4 eV ($\varepsilon = 12\,000$ L cm^{-1} mol^{-1}). We felt comfortable assigning

the peak at 3.3 eV to the lowest LMCT band, given its large extinction coefficients and because the TDDFT calculations of the optical spectrum yielded states with appreciable intensity at 2.9 eV and another at >4 eV. This information was useful for our CTM4XAS calculations, in that it provided upper bounds on acceptable values for ΔE_{gs} and T_{gs}. In particular, the energy of the LMCT band should be of the order of $\Delta E_{gs} + 2T_{gs}$. In addition, an NBO analysis of our ground state DFT calculations gave an effective hopping integral of roughly 1.1 eV. Combined, this information severely restricted our parameter space. Hence, we found that $\Delta E_{gs} = 2.5$ eV and $T_{gs} = 0.7$ eV resulted in a calculated output LMCT of 3.6 eV, which was in reasonable agreement with the direct UV−vis measurement. Within these constraints, our calculated ground state was modeled roughly with 75% $3d^{10}4f^0$ and 25% $3d^{10}\underline{L}4f^1$. We note once again that this description is in the atomic orbital representation, and can be rewritten in terms of a molecular orbital of similar parentage with Ln 4f- and Cl 3p-orbital mixing in the ground state. It does not imply a strong ground state correlation effect.

The remaining parameter to specify for the XAS calculation was ΔE_{fs}. This is defined by the model as $\Delta E_{fs} = \Delta E_{gs} + U_{ff} - U_{fd}$, where U_{ff} and U_{fd} represent the self-repulsion and core Coulombic repulsion integrals, respectively. In L-edge spectra from transition metals, the self-repulsion is often ~2 eV smaller than core repulsion. In general, the Hubbard U_{ff} is notoriously large in lanthanides because of the small orbital radius. However, as de Groot has pointed out previously, generally the core−valence repulsion (U_{fd}) is somewhat larger than the self-repulsion (U_{ff}). This indeed occurred in our calculations for $CeCl_6^{2-}$, as a very good fit to the $M_{5,4}$-edge XAS experimental data was obtained with $\Delta E_{fs} = -1.5$ eV. Note this value for ΔE_{fs} suggested that, in the presence of the core−hole, the effective final state charge transfer energy was significantly reduced, in this case becoming negative in value. Hence, the ground state includes a degree of covlanecy between the Ce 4f- and Cl 3p-orbitals, while the structure in the final state is assigned to a final state configuration interaction. Note that the latter reflects a change in covalency in the final state induced by the presence of the 3d core-hole. A more detailed study of our modeling will be presented in the future, and more work is needed to test the generality of our conclusion and the implications on the origins of the Ce^{IV} M-edge XAS features.

Finally, we remind the reader that the parameters used for $CeCl_6^{2-}$ (formally Ce^{IV}) were quite consistent with what was

used in the $CeCl_6^{3-}$ (formally Ce^{III}) model. The distinguishing characteristic in the Ce^{III} case was that the initial state charge transfer energy was significantly increased relative to Ce^{IV}. This was because for $CeCl_6^{3-}$, the ΔE_{gs} (Ce^{III}) = $E(3d^{10}\underline{L}4f^2)$ − $E(3d^{10}4f^1)$ + U_{ff} was significantly larger than the ΔE_{gs} for $CeCl_6^{2-}$ (Ce^{IV}), owing to the large Coulomb repulsion associated with Ce^{III} charge transfer. As a result, the Ce^{III} ground state was firmly in the atomic limit, which was consistent with our DFT results that suggested no spin delocalization and that the spin density on the Ce^{III} (1.0) was identical to the value expected in the ionic limit.

$LnCl_6^{x-}$ Cl K-Edge XAS. The background-subtracted and normalized Cl K-edge XAS spectra obtained from $CeCl_6^{2-}$ and $LnCl_6^{3-}$ (Ln = Ce, Nd, Sm, Eu, Gd) are compared in Figure 10.
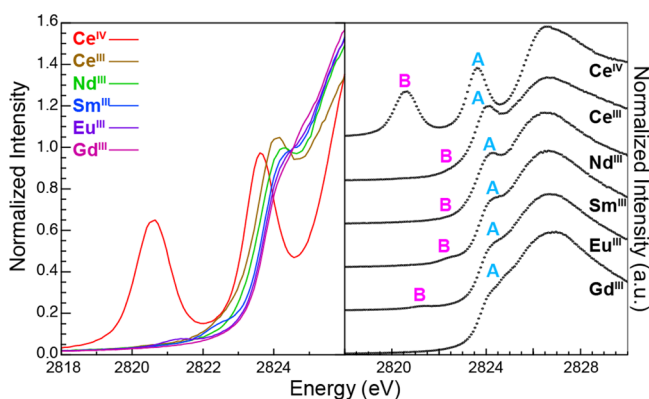
Figure 10. Overlay of the background-subtracted and normalized Cl K-edge XAS spectra for $CeCl_6^{2-}$ and $LnCl_6^{3-}$ (Ln = Ce, Nd, Eu, Sm, and Gd).

In many ways, the Cl K-edge XAS spectra from these hexachlorides were quite similar. Most obviously, a dominant edge peak near 2826 eV superimposed on a step-like absorption threshold primarily characterized the spectra (see Supporting Information). More subtle attributes common to each spectrum included pre-edge features that were indicative of covalent Ln−Cl bonding (<2825 eV). A deconvoluted model was obtained for the $CeCl_6^{2-}$ and $LnCl_6^{3-}$ Cl K-edge XAS spectra as shown in Figure 11, summarized in Table 2, and described in the Experimental Section. Overall, this approach provided high-quality models of the data, as evidenced by good correlation coefficients and symmetric residual peaks that were similar in shape to the corresponding pseudo-Voigt functions. Additionally, the residuals in each spectrum were less than 2% from 2818 to 2830 eV.

To evaluate the $LnCl_6^{x-}$ Cl K-edge XAS spectra, we found it convenient to begin the discussion with $CeCl_6^{2-}$ (formally Ce^{IV}). Parameters from the curve-fitting analysis of the $CeCl_6^{2-}$ spectrum showed a large pre-edge feature near the onset of the rising edge at 2823.6 eV (aqua trace, A-feature in Figure 10) and a second low-energy feature at 2820.6 eV (B-feature in Figure 10; pink trace in Figure 11). Both features were well resolved from the rising edge, which had an inflection point of 2825.7 eV. The large peak area (defined hereafter as peak intensity) of 0.70(7) for the B-feature was comparable to that of the A-feature at 0.84(8). The spectra from the $LnCl_6^{3-}$ (formally Ln^{III}) were similar to that obtained from $CeCl_6^{2-}$ in that they also contained intense A-features near the rising edge (~2824 eV; aqua trace in Figure 11) with intensities ranging from 0.93(9) to 0.48(5).
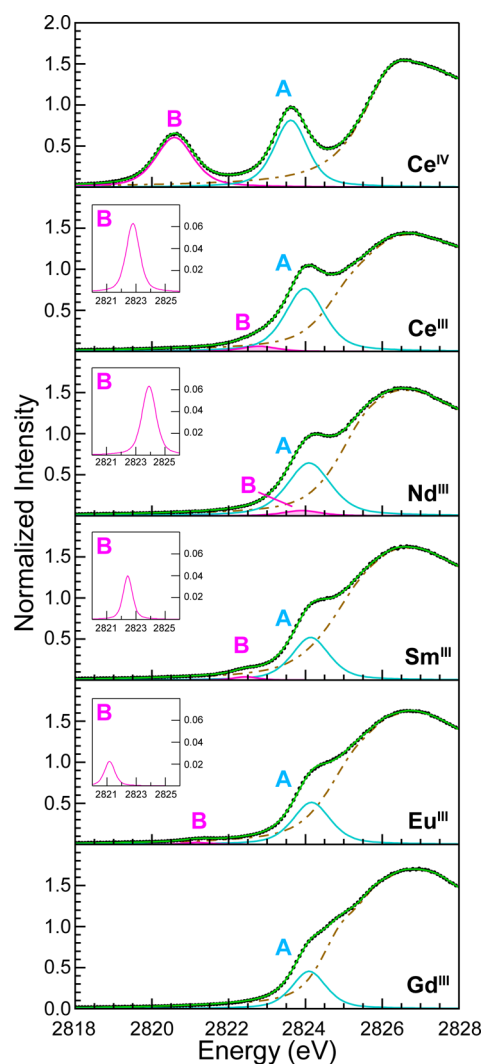
Figure 11. Cl K-edge XAS experimental data (○) obtained from the Z_3LnCl_6 (Ln = Nd, Sm, Eu, Gd and Z = NEt_4; Ln = Ce and Z = PPh_4) and $(NEt_4)_2CeCl_6$ compounds. The pre-edge pseudo-Voigt functions (aqua and pink traces) used to generate the deconvoluted spectra (green trace) are included. The functions used to describe the edge-region of the Cl K-edge XAS spectra are summed to give the brown dashed trace. Feature B from Figure 10 is provided in the cut-out.

Because the A-features were quite close to the rising edge in the $LnCl_6^{3-}$ (formally Ln^{III}) spectra, care was taken to maintain consistency in modeling the edge region (2818−2830 eV). The cautious approach to modeling of the rising edge line shape allowed changes in A-feature peak intensities to be evaluated as a function of metal identity, from Ce^{III} to Gd^{III}. As shown by the dashed brown trace in Figure 11, which represented the summation of functions used to model the spectral edge regions (>2825 eV; fully deconvoluted spectra provided in the Supporting Information), the rising edge line shape deviated only slightly from Ce^{III} to Gd^{III}. For instance, the rising edge position was constant for all the data, as evidenced from the first inflection point varying by only 0.47 eV. Additionally, the slope of the rising edges (dashed brown trace, Figure 11) was nearly equivalent for all of the trivalent hexachlorides (average slope = 0.57 with a standard deviation of ±7.0%). These results suggested that changes in relative intensity for the pre-edge A-features could be determined with confidence despite their proximity to the rising edge. Error in the A-feature peak

Table 2. Comparison of the Experimental Cl K-Edge XAS Pre-edge Peak Energies, Intensities, Amounts of Cl 3p-Character, and TDDFT Calculated Oscillator Strengths (f) Associated with Electronic Excitations from Cl 1s-Orbitals to the $t_{2g}*$ and $t_{2u}* + t_{1u}*$ Orbitals for the Z_3LnCl_6 (Ln = Nd, Sm, Eu, Gd and Z = NEt$_4$; Ln = Ce and Z = PPh$_4$) and (NEt$_4$)$_2$CeCl$_6$ Compounds

assignment	energy (eV)	intensity (exp)	Cl 3p/bond (%) exptl	Cl 3p/bond (%) calcd[a]	TDDFT f, ×1000
O_h-CeCl$_6{}^{2-}$					
Cl 1s→$t_{2g}*$	2823.6	0.84(8)	11(1)	6.0	4.90
Cl 1s→4f	2820.6	0.70(7)	9.9(9)	15.5	5.50
O_h-CeCl$_6{}^{3-}$					
Cl 1s→$t_{2g}*$	2824.0	0.93(9)	13(1)	3.9	3.90
Cl 1s→4f	2822.8	0.07(2)	1.0(3)	2.7	1.30
O_h-NdCl$_6{}^{3-}$					
Cl 1s→$t_{2g}*$	2824.1	0.83(8)	12(1)	3.9	3.98
Cl 1s→4f	2823.8	0.07(2)	1.0(3)	3.8	1.33
D_{4h}-SmCl$_6{}^{3-}$					
Cl 1s→$e_g*+b_{2g}*$	2824.1	0.60(6)	8.5(9)	3.7	3.95
Cl 1s→4f	2822.4	0.03(1)	0.4(1)	1.1	1.30
D_{4h}-EuCl$_6{}^{3-}$					
Cl 1s→$e_g*+b_{2g}*$	2824.2	0.59(6)	8.4(8)	4.3	4.61
Cl 1s→4f	2821.2	0.02(3)	0.3(3)	6.4	1.99
O_h-GdCl$_6{}^{3-}$					
Cl 1s→$t_{2g}*$	2824.1	0.48(5)	6.8(7)	3.3	3.75
Cl 1s→4f	–	–	–	2.4	0.013

[a] The calculated Cl 3p/bond values were determined by multiplying the total Cl 3p-character from the Mulliken populations by the sum of the squares of the normalization constants for the corresponding ligand-orbital wave functions (see Experimental Section).

intensity was estimated at 10% based on our ability to reproduce the data on beamlines 6-2 and 4-3 at the Stanford Synchrotron Radiation Lightsource (SSRL) synchrotron as well as at the Institut für Nukleare Entsorgung (INE) beamline at the Angströmquelle Karlsruhe (ANKA) synchrotron during multiple experimental periods.

Our curve-fitting models suggested that the intensity for the A-features systematically decreased as a function of lanthanide metal identity (Ce^{III} to Gd^{III}), which corresponded with an increase in the effective nuclear charge of the metal (Z_{eff}). For example, although the intensities of 0.93(9) for Ce^{III} and 0.83(8) for Nd^{III} were equivalent once the error was considered (Table 2 and Figure 11), marked intensity decreases were observed when non-adjacent lanthanides on the periodic table were compared. The most extreme example was associated with the decrease from 0.93(9) in Ce^{III} to 0.48(5) for Gd^{III}. Given that the pre-edge peak intensities are directly related to the degree of Ln−Cl orbital mixing, these results suggested that M−Cl covalency decreased systematically with increasing Z_{eff} across the lanthanide series. As a reminder, the structural analysis provided in Table 1 showed no evidence of such changes.

The Cl K-edge XAS spectra from the LnCl$_6{}^{3-}$ (formally Ln^{III}) differed from that of CeCl$_6{}^{2-}$ (formally Ce^{IV}) in that the Ln^{III} B-features were quite small and best described as shoulders at the base of the A-features. Comparisons within the LnCl$_6{}^{3-}$ (formally Ln^{III}) series revealed subtle differences. For instance, while the energies of the A-features (2824 eV) and edge-peaks (2827 eV) remained relatively constant as the

lanthanide series was traversed from Ce^{III} to Gd^{III}, close inspection revealed systematic variations between spectra. In general, moving to the right of Ce^{III} on the periodic table caused the energy for the B-feature to broaden and shift to lower energy until it disappeared into the baseline of the GdCl$_6{}^{3-}$ spectrum. In contrast to CeCl$_6{}^{2-}$ (formally Ce^{IV}), where both the A- and B-features could be evaluated with confidence, the low intensity of the B-features associated with the LnCl$_6{}^{3-}$ challenged the sensitivity of the experiment. Despite these issues, the data in Figure 11 were best modeled for Ce^{III}, Sm^{III}, and Eu^{III} with an unconstrained B-feature. To obtain a model for Nd^{III} that could be compared directly with Ce^{III}, Eu^{III}, and Sm^{III}, the peak height and width for the Nd^{III} B-feature had to be constrained between that observed for Ce^{III} and Eu^{III}. The error associated with the Nd^{III} B-feature overlapped with that of Ce^{III} and Eu^{III} and, in general, uncertainties in the intensity for all of the LnCl$_6{}^{3-}$ B-features were estimated to be quite high. Hence, although we acknowledge the presence of B-features and while the data suggests that B-features were quite small, we refrain from attempting to quantify the B-feature intensities.

LnCl$_6{}^{x-}$ Ground-State Electronic Structure. Density functional theory (DFT) calculations were conducted on the LnCl$_6{}^{x-}$ anions at their optimized geometries. This computational effort included Pr^{III} and Pm^{III}, which were not experimentally evaluated. Unrestrictive Kohn−Sham calculations were carried out using relativistic effective core potentials (RECPs) on the high-spin ground states (Hund's first rule). The computational results for the α spin−orbitals are summarized in Table 3, as well as in the quantitative orbital level diagram shown in Figure 12. We have limited this discussion to only unoccupied orbitals relevant to the XAS experiments (Scheme 2) because the electronic structures for O_h-LnCl$_6{}^{x-}$ anions have been previously described.[18,123−126] Results from our DFT calculations were consistent with group theoretical considerations and were summarized as follows. For O_h-LnCl$_6{}^{x-}$ anions, a symmetry-adapted linear combination (SALC) of six Cl 3p-atomic orbitals having σ-symmetry with respect to the Ln−Cl bond spanned $a_{1g} + e_g + t_{1u}$ symmetries. There were also 12 Cl 3p-SALCs with π-symmetry with respect to the Ln−Cl bond that transformed as $t_{1g} + t_{2g} + t_{1u} + t_{2u}$. With this designation, the Ln 5d-orbitals were allowed by symmetry to mix and form Ln−Cl σ- and π-interactions of e_g and t_{2g} symmetries, respectively, which is well established for the MCl$_6{}^{x-}$ transition metal analogues.[7,127−132] Superimposed on this orbital picture (and at lower energy) was the Ln 4f-manifold, which in an octahedral ligand field transformed with $a_{2u} + t_{2u} + t_{1u}$ symmetries. Hence, the Ln 4f-orbital of a_{2u} symmetry was rigorously nonbonding, the t_{2u} orbitals formed Ln−Cl π-interactions, and the t_{1u} orbitals formed Ln−Cl σ- and π-interactions. This left the Cl t_{1g} orbitals as nonbonding Cl lone pair orbitals.

It is in this orbital framework that the experimental XAS spectra were interpreted. Moving from Ce^{IV} to Ce^{III} then to Gd^{III} resulted in successive filling of the 4f-orbitals, such that there was not double occupancy in any of the calculated ground states. The orbital description in O_h-symmetry (described above) was in good agreement for the closed-shell CeCl$_6{}^{2-}$ and GdCl$_6{}^{3-}$ systems and for CeCl$_6{}^{3-}$ and NdCl$_6{}^{3-}$, where the a_{2u} and t_{1u} orbitals were half-filled. However, for PrCl$_6{}^{3-}$, PmCl$_6{}^{3-}$, SmCl$_6{}^{3-}$, and EuCl$_6{}^{3-}$ the calculations converged to D_{4h} structures with slight changes in the axial and equatorial bond distances. This structural distortion was small with the standard

Table 3. Calculated Atomic Compositions of Selected Molecular Orbitals for the Z_3LnCl_6 (Ln = Nd, Sm, Eu, Gd and Z = NEt$_4$; Ln = Ce and Z = PPh$_4$) and $(NEt_4)_2CeCl_6$ Compounds[a,b,c]

MO	energy (eV)[c]	composition (%)			MO	energy (eV)[c]	composition (%)		
		Cl 3p	Ln 5d	Ln 4f			Cl 3p	Ln 5d	Ln 4f
		O_h-CeCl$_6^{3-}$					O_h-PmCl$_6^{3-}$		
e_g*	9.27	9.9	92.2	0.0	e_g*	8.95	11.6	90.2	0.0
t_{2g}*	7.32	5.2	94.0	0.0	t_{2g}*	7.18	5.2	93.8	0.0
t_{2u}*	6.44	0.4	0.0	99.4	t_{2u}*	3.88	1.2	0.0	98.8
t_{1u}*	5.96	1.8	0.0	97.5	t_{1u}*	−2.89	2.4	0.0	97.5
a_{2u} (nb)	0.96	0.0	0.0	100.0	a_{2u} (nb)	−3.56	0.0	0.0	100.0
		D_{4h}-PrCl$_6^{3-}$					D_{4h}-EuCl$_6^{3-}$		
b_{1g}*	9.19	10.8	91.7	0.0	b_{1g}*	9.65	8.4	85.7	0.0
a_{1g}*	9.12	10.6	91.7	0.0	a_{1g}*	9.56	9.2	83.6	0.0
e_g*	7.33	5.0	94.1	0.0	b_{2g}*	8.44	5.6	94.1	0.0
b_{2g}*	7.24	5.2	93.9	0.0	e_g*	8.27	5.8	93.8	0.0
a_{2u}*	5.96	1.6	0.0	97.7	a_{2u}*	1.75	24.8	0.0	75.0
b_{1u} (nb)	5.76	0.0	0.0	100.0	e_u*	−2.88	1.2	0.0	98.8
$2e_u$*	5.14	2.2	0.0	97.2	b_{2u}*	−3.15	0.4	0.0	99.7
b_{2u}*	4.80	0.8	0.0	99.1	b_{1u} (nb)	−3.16	0.0	0.0	100.0
$1e_u$*	−0.61	16	0.0	84.1	e_u*	−4.10	0.4	0.0	99.5
		O_h-NdCl$_6^{3-}$					O_h-GdCl$_6^{3-}$		
e_g*	9.11	11.0	91.0	0.0	e_g*	9.17	9.8	92.5	0.0
t_{2g}*	7.28	5.2	94.0	0.0	t_{2g}*	7.50	4.4	94.8	0.0
a_{2u} (nb)	4.97	0.0	0.0	100.0	t_{2u}*	−3.10	0.4	0.0	99.6
t_{2u}*	4.77	2.0	0.0	97.4	a_{2u} (nb)	−3.10	0.0	0.0	100.0
t_{1u}*	−1.90	2.6	0.0	97.5	t_{1u}*	−3.13	1.4	0.0	98.4
		D_{4h}-SmCl$_6^{3-}$					O_h-CeCl$_6^{2-}$		
b_{1g}*	9.20	11.6	90.5	0.0	e_g*	9.38	18.0	86.9	0.0
a_{1g}*	9.15	1.4	90.5	0.0	t_{2g}*	6.82	8.0	90.4	0.0
e_g*	7.35	4.8	94.0	0.0	t_{1u}*	3.19	9.9	0.0	89.6
b_{2g}*	7.34	5.2	94.0	0.0	t_{2u}*	3.18	3.2	0.0	96.8
e_u*	3.32	4.6	0.0	95.1	a_{2u} (nb)	3.11	0.0	0.0	100.0
b_{1u} (nb)	−2.55	0.0	0.0	100.0					
e_u*	−2.95	0.8	0.0	99.3					
b_{2u}*	−3.68	0.4	0.0	99.7					
a_{2u}*	−3.78	0.1	0.0	98.8					

[a]Alpha spin−orbital energies are reported. [b]The use of a non-orthogonal basis set can cause Mulliken analysis to have nonphysical results such as compositions >100% or <0.[166] [c]The calculated values are normalized to the t_{1g}-symmetric highest occupied molecular orbital of CeCl$_6^{2-}$.

deviation from the mean varying between 0.004 and 0.7% from the calculated values (Table 1). Hence, the calculated distances were still in agreement with the experimental structures but consistent with a Jahn−Teller distortion. In the text that follows, orbitals from the D_{4h}-LnCl$_6^{3-}$ calculations were discussed using symmetry labels for the parent O_h-orbitals. Overall, the calculated systematic variation in orbital composition and energy was in relatively good agreement with experimental observations, suggesting that these calculations provided an appropriate guide for interpreting the Cl K-edge XAS spectra.

Spectral Interpretation. To guide our spectral interpretations, TDDFT calculations were used to simulate the LnCl$_6^{x-}$ Cl K-edge XAS spectra. Analogous computational methods were previously employed to model spectra for several other transition metal and actinide systems and had good experimental agreement.[6−8,57−60,66−68,133−135] Before discussing the results in detail, we found it pertinent to discuss several caveats that were particularly relevant in this series. To provide guidance for experiment, it was useful to stay as close as

possible to a one-electron orbital picture. The neglect of the spin−orbit interaction in our calculations was a first concern, but previous experience with actinide compounds[136] suggested it would not qualitatively change the comparison of theory and experiment. A greater concern was associated with the fact that the TDDFT calculation provided a single particle−hole approximation, and that the *full* manifold of final states associated with the core−hole excitation was not addressed. To best understand what was included versus omitted in the calculations, consider the ionic limit where all the f-orbitals were localized on the metal. If the ground state was f^i, then the excited state would be associated with the configuration f^{i+1}. In this scenario, there are several ways to couple the orbital and spin angular momenta of the states arising from f^{i+1}, each leading to a different final state multiplet. For instance, in the case of an f^2 ground state (Hund's rule suggests S = 1, L = 5, or ^{3}H), excitation of a Cl 1s electron would lead to an f^3 configuration. Hence, there would be three spin states associated with three unpaired electrons, a quartet and two doublets. There would also be a number of angular momentum
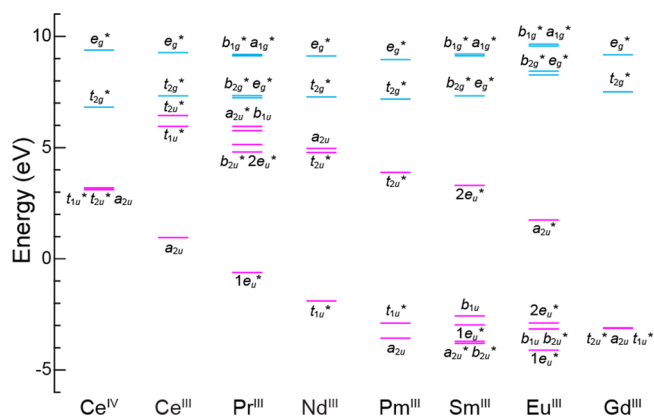
Figure 12. Orbital diagram of α orbitals from DFT ground-state calculations for the $LnCl_6^{x-}$ (Ln = Ce, x = 2; Ln = Ce, Pr, Nd, Pm, Sm, Eu, Gd, x = 3) anions. Orbitals containing primarily 5d- (blue lines) and 4f-character (pink lines) are shown. In the calculations, the symmetry was reduced from O_h to D_{4h} for Pr^{III}, Sm^{III}, and Eu^{III}, owing to Jahn–Teller distortions. The calculated values are normalized to the highest occupied t_{1g}-symmetric orbital of $CeCl_6^{2-}$.

**Scheme 2. Relevant Unoccupied Kohn–Sham Orbitals That Have Primarily 5f- or 6d-Character for $CeCl_6^{2-}$**
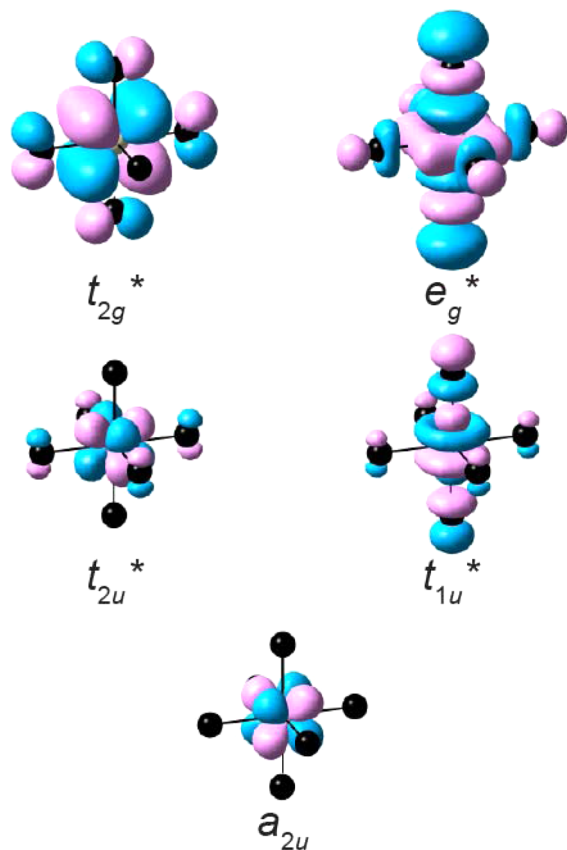
couplings available to the three unpaired electrons. To fully address the states associated with this configuration requires *multielectron* excitations relative to the single determinant describing the ^3H ground state. However, our TDDFT calculations generate only *single* particle–hole excitations and are therefore not able to describe all these final states. In particular, for the f^2 ground state the TDDFT allowed excitations yield a quartet and only one doublet. The energy

of this doublet state is an average of the two actual doublet states and the oscillator strength a similar average. Nevertheless, this crude TDDFT particle–hole approximation has been effective in the past for assigning the spectra.

The computational results are compared with the experimental data in Figure 13 and Table 2. In Figure 13, the total
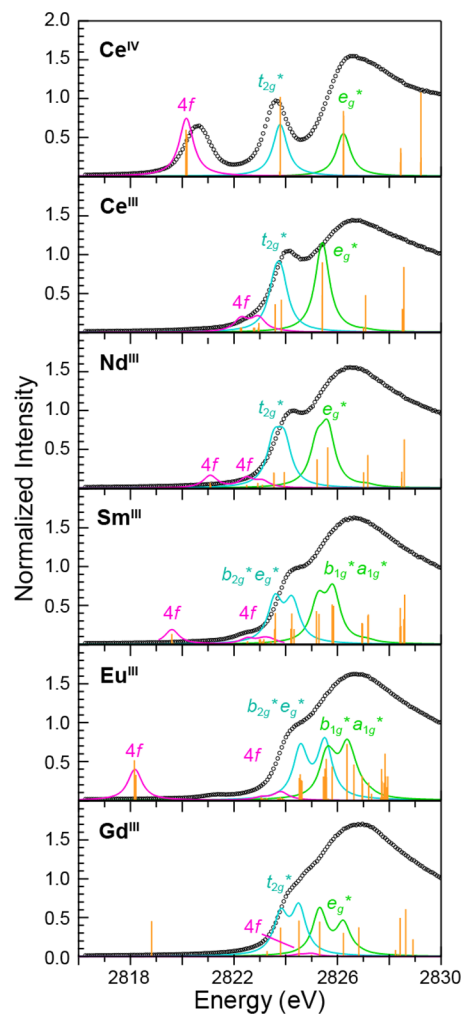
Figure 13. Comparison between experimental Cl K-edge spectra (○) and results from the TDDFT calculations for the $LnCl_6^{x-}$ (Ln = Ce, x = 2; Ln = Ce, Nd, Sm, Eu, Gd, x = 3) anions. The orange bars represent the energy and oscillator strength for the calculated transitions. The partial densities of states derived from the TDDFT for final states associated with 4f- (pink trace) and 5d- orbitals (aqua and green traces) are also shown.

TDDFT output has been represented by orange bars and the partial density of 4f-states derived from the TDDFT calculations were shown using pink traces, while t_{2g}^* and e_g^* states were represented by aqua and green traces. For D_{4h}-$LnCl_6^{3-}$ anions, states of t_{2g}^* and e_g^* parentage in O_h-symmetry were also shown using aqua and green traces, respectively. Each calculated spectrum has been shifted by a uniform +64 eV to account for omission of electronic relaxations and other effects (see Experimental Section).[137,138] In general, the calculations agreed well with the experimental data and were consistent with expectations based on group theory analyses. For example, assuming that only transitions associated with electric dipole-allowed final states will be observed by Cl K-edge XAS
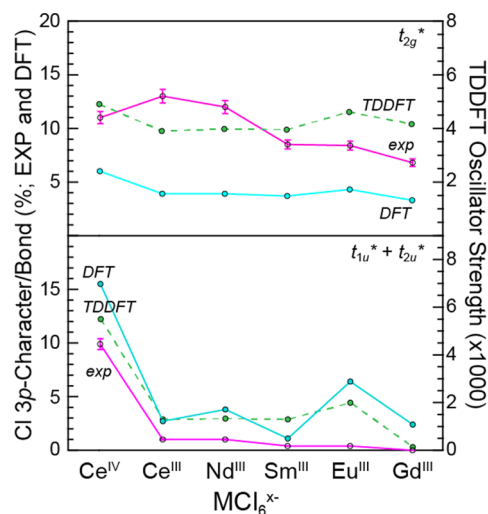
spectroscopy, we anticipated only transitions from the $^1A_{1g}$ ground-state to $^1T_{1u}$ final states for a $4f^05d^0$ O_h-LnCl$_6$$^{x-}$ anion (dipole operator t_{1u}). As such, the TDDFT calculations showed electronic excitations from Cl 1s-orbitals to unoccupied orbitals that resulted from mixing between Cl 3p-orbitals and either the Ln 4f- (in O_h symmetry orbitals of t_{1u}* and t_{2u}* symmetries) or 5d-orbitals (in O_h symmetry t_{2g}* and e_g*). Thus, for the LnCl$_6$$^{x-}$ anions (formally containing Ln^{III} and Ce^{IV}), the TDDFT results attributed the low-energy B-feature to overlapping electronic excitations from Cl 1s-orbitals to orbitals of t_{1u}* and t_{2u}* symmetries (pink trace), which were primarily of Ln 4f character. Higher energy A-features were primarily associated with Cl 1s electronic excitations to 5d π-orbitals (aqua trace; t_{2g}* in O_h-symmetry), while transitions associated with the 5d σ-orbitals (e_g* in O_h-symmetry) were calculated to be buried beneath the rising edge (green trace).

In support of this spectral interpretation, both experiment and theory agreed in trends observed for 4f- and 5d-orbital energies. For example, while transitions to the t_{2g}* (probed by XAS and DFT) and e_g* (DFT only) orbital energies remained constant, the energy for both the singly occupied and unoccupied 4f-orbitals decreased as the central ion identity was changed from Ce^{IV} to Nd^{III}, Sm^{III}, and Eu^{III}. These trends in 4f- and 5d-orbital/transition energies were reasonably rationalized using Slater's rules.[139] The energy range for the calculated transitions involving 4f-orbitals also increased for Ce^{III} to Nd^{III}, Sm^{III}, and Eu^{III}. This broadening was largely attributed to the multiplets resulting from the increase in 4f-electron count. Unfortunately, we could not use Cl K-edge XAS to confirm this observation because of the low-intensity and poorly resolved pre-edge B-features. We anticipated that larger energy broadening would be computationally observed once spin−orbit effects were considered, and future efforts are focused on incorporating these contributions into our theoretical model. For Gd^{III}, a resolved low-energy B-feature was not observed experimentally. Consistently, the calculations indicated that transitions involving the 4f-orbitals were pushed high in energy, as exciting a Cl 1s electron to the half-filled Gd $4f^7$-manifold was accompanied by electronic repulsion resulting from the double occupancy in the final state. The only transition calculated at low energy (near 2819 eV) was associated with an a_{1g} (5s of Rydberg type) orbital, but a corresponding pre-edge feature was not observed experimentally.

Ln−Cl Orbital Mixing. It has been established that the transition intensities observed for the pre-edge peaks in Cl K-edge XAS spectra are directly related to the amount of Cl 3p character in M−Cl bonds.[48] Hence, the LnCl$_6$$^{x-}$ data described above offers an opportunity to quantify changes in Ln 4f- and 5d-covalency as a function of (1) the lanthanide metal identity and (2) the lanthanide oxidation state. To directly compare the experimental and DFT results, we used the well-defined Cs$_2$CuCl$_4$ Cl K-edge XAS intensity standard to convert experimental pre-edge peak intensities to the amount of Cl 3p-character (%) per Ln−Cl bond (an intensity of 0.53 = 7.5% Cl 3p-character per bond).[48,140] Similarly, the amount of Cl 3p-character determined from the Mulliken population analysis was converted to a per-bond basis as described previously and outlined in the Experimental Section.[7] As described subsequently, there were appreciable differences in the experimental pre-edge peak intensities, which in turn indicated that the amount of Ce^{IV}−Cl and Ln^{III}−Cl orbital mixing varied substantially. These experimental observations were consistent

with the DFT and TDDFT calculations, and could not have been anticipated on the basis of the structural analyses described above.

It is instructive to begin by considering only the Ln−Cl 5d-interactions (top panel in Figure 14 and Table 2). For all

Figure 14. Comparison of amount of Cl 3p-character per bond determined using Cl K-edge XAS (pink, left axis), Mulliken orbital population analyses (blue, left axis), and TDDFT (dashed green, right axis). The top panel shows values for the 5d-orbital of t_{2g}* symmetry, and the summation for the 4f-orbitals is provided in the bottom panel.

LnCl$_6$$^{x-}$ (x = 2, 3) analytes probed, significant amounts of Cl 3p-character were experimentally determined in the 5d π-orbitals of t_{2g} symmetry. These experimental values ranged from 7 to 13% per Ln−Cl bond and were in reasonable agreement with those determined from the Mulliken population analysis of the ground-state DFT calculations (ranging from ∼3 to 4%). Across the lanthanide series, both the DFT and TDDFT (Figure 14) calculations showed virtually no change in the amount of Cl 3p-character in orbitals of t_{2g}* symmetry (in the D_{4h}-point group, orbitals of t_{2g}* parentage). Meanwhile, the experimental measurement indicated a decrease in Ln−Cl t_{2g} orbital mixing from Ce^{III} to Gd^{III}. When the experimental error was considered, changes between adjacent Ln^{III}-containing compounds were indiscernible while a substantial decrease in Ln−Cl t_{2g}* orbital mixing was apparent when comparing Ce^{III}, 13(1)%, and Gd^{III}, 6.8(7)% (Table 2, Figure 14). It was unclear if this difference between theory and experiment was associated with our computational model or with a systematic experimental bias associated with resolving the t_{2g}* pre-edge feature (A-feature in Figure 4). For the 5d σ-orbitals (e_g*), experimental values could not be determined, owing to the proximity of these transitions to the rising edge. However, we could evaluate the DFT results. In this case, as observed for the t_{2g}* orbitals, the calculations indicated that changing the metal from Ce^{III} to Gd^{III} had little effect on the amount of Cl 3p-character in the e_g* orbitals, which fluctuated between 2.9 and 3.8%.

The influence of lanthanide oxidation state on orbital mixing in the 5d π-orbitals (t_{2g}*) was also investigated by comparing CeCl$_6$$^{3-}$ with CeCl$_6$$^{2-}$ (Figure 14 and Table 2). Oxidizing CeCl$_6$$^{3-}$ to CeCl$_6$$^{2-}$ only slightly decreased the amount of Cl 3p-character from 13(1) to 11(1)% observed experimentally; however, these values were equivalent within error. These data

compared well with the analogous calculated values of 3.9 and 6.0%. Overall, the results indicated that the change from formally Ce^{III} to Ce^{IV} had little effect on the amount of Cl 3p- and Ce 5d-orbital mixing.

In regard to 4f-orbital mixing (bottom panel, Figure 14), both theory and experiment were in reasonable agreement. For the $LnCl_6^{3-}$ (formally Ln^{III}), both experimental and DFT analyses provided unambiguous evidence that the 4f-orbitals participated in weak covalent bonding and were significantly less engaged than the 5d-orbitals of $t_{2g}*$ symmetry (in the D_{4h}-point group, orbitals of $t_{2g}*$ parentage). Our results for the $4f^1$ $CeCl_6^{3-}$, which showed only 1(1)% Cl 3p-character per Ln−Cl bond, were in reasonable agreement with the analysis by Edelstein and Lukens using UV−vis spectroscopy that also showed only marginal involvement of the t_{1u} and t_{2u} orbitals in Ce^{III}−Cl bonding.[141] Moving across the lanthanide series from left to right, both experiment and theory indicated that the energy of the orbitals decreased while the amount of Cl 3p-character determined in the combined 4f-orbitals remained relatively constant (Figure 14 and Table 2). The DFT-determined amount of Cl 3p-character per bond in the 4f-orbitals fluctuated between 1.1 and 3.8% for Ce^{III}, Nd^{III}, Sm^{III}, and Gd^{III}, while the calculated value for Eu^{III} $4f^6$ was increased to 6.4%.

While the amount of Ln^{III}−Cl mixing was experimentally and computationally found to be small, oxidizing Ce^{III} to Ce^{IV} showed unambiguous evidence for pronounced Ce 4f- and Cl 3p-orbital mixing. For instance, the amount of Cl 3p-character per Ce−Cl bond in the t_{1u} and t_{2u} orbitals was experimentally determined to be 9.9(9)%, which was similar to the 15% value determined by DFT. The pronounced Ce−Cl orbital mixing observed in $CeCl_6^{2-}$ (formally Ce^{IV}) is reasonable given the uniqueness of Ce^{IV} in comparison to the rest of the trivalent lanthanides; e.g., the atomic configuration for Ce^{IV} is $[Xe]4f^1 5d^1 6s^2$. These values were comparable to previous measurements made on transition metal and actinide hexahalides and the Ce^{IV}−Cl uniqueness has been addressed in more detail in the following section. Despite the relatively good agreement between experiment and theory for all of the Ln−Cl interactions probed here, in general, the DFT calculations slightly overestimated the amount of Ln−Cl orbital mixing for 4f-orbitals and underestimated the participation of the 5d-orbitals. Previous studies on actinide 5f- and Cl 3p-orbital mixing provided similar results.[6,7]

■ OUTLOOK AND CONCLUDING REMARKS

These results have shown that Cl K-edge XAS can be used to evaluate both Ln 4f- and 5d-orbital mixing with Cl 3p-orbitals in Ln−Cl bonds. Weak pre-edge features associated with transitions to π and $\sigma + \pi$ orbitals of primarily 4f-character ($t_{1u}*$ and $t_{2u}*$ in O_h-symmetry) were observed by Cl K-edge XAS and TDDFT that suggested only marginal involvement of the 4f-orbitals in Ln^{III}−Cl bonding (Ln = Ce^{III}, Nd^{III}, Sm^{III}, Eu^{III}, Gd^{III}). Both theory and experiment indicated that moving across the lanthanide series (from Ce^{III} to Gd^{III}) dropped the overall energy of the 4f-manifold, while the amount of Ln 4f- and Cl 3p-orbital mixing remained small and relatively constant. In contrast, we observed appreciable mixing between the Ln 5d- and Cl 3p-orbitals, as was evident from the measured and calculated amounts of Cl 3p-character in the π-bonding $t_{2g}*$ orbitals, which ranged from 6.8(7) to 13(1)% by Cl K-edge XAS and from 3.3 to 4.3% by DFT. Although the σ-bonding e_g* orbitals could not be probed experimentally, the

calculated values (3.3−3.8%) also suggested that Ln 5d and Cl 3p σ-orbital mixing occurred in the $LnCl_6^{x-}$ anions. In comparison to the trends described above for the Ln 4f-orbitals, our results indicated that systematically changing the metal identity from Ce^{III} to Gd^{III} had very little effect on the $t_{2g}*$ and e_g* (primarily 5d) orbital energies. In terms of $t_{2g}*$ orbital compositions, the experimental values showed a decrease in Cl 3p-character from Ce^{III} to Gd^{III}, while the DFT and TDDFT calculations showed no appreciable change. One explanation that accounted for this discrepancy came from the TDDFT analyses, which suggested that for Sm^{III}, Eu^{III}, and Gd^{III} the $t_{2g}*$ peaks broadened, likely resulting from increased multiplet effects. We additionally anticipate further broadening from SOC, which was not included in the TDDFT calculations. If this calculated range of transitions is correct, it is possible that additional pre-edge peak intensities are masked within the rising absorption edge and that the experimental measurements did not provide the entire picture. Hence, future efforts are focused on determining if experimental conditions can be identified that provide better resolution for these $t_{2g}*$ pre-edge peaks and confirm that Ln 5d- and Cl 3p-orbital mixing decreased from Ce^{III} to Gd^{III}.

Changing from $CeCl_6^{3-}$ to $CeCl_6^{2-}$ had a surprising influence on Ce−Cl covalent mixing. Increasing the Ce oxidation state—in essence—"turned on" Ce 4f- and Cl 3p-orbital mixing, such that both experiment and theory showed that the amount of Cl 3p-character in the $t_{2u}* + t_{1u}*$ (4f) orbitals was comparable to that in the $t_{2g}*$ or e_g* (5d) orbitals. Although we have not characterized the generality of this observation, it seems likely that this is not an isolated case, and we assume that 4f-orbital participation in covalent bonding occurs in other systems. In transition metal chemistry, a similar observation has been made for high-temperature super-conducting cuprate materials.[142] In this case the Cu^{II} d^9 ground state is reasonably ionic in character; however, upon hole doping, the effective "Cu^{III}" site has significantly increased hybridization with O 2p orbitals. Once again, Cu^{II} is more ionic than Cu^{III} due to the rather large U_{dd} parameter associated with the dd repulsion in the LMCT final state ($\underline{L}d^{10}$) in Cu^{II}. The striking difference in covalent Ce^{IV}−Cl vs Ce^{III}−Cl bonding could not be predicted on the basis of the structural metrics obtained from the single-crystal XRD measurements. Hence, these results clearly caution against using Shannon ionic radii and structural metrics to infer conclusions regarding electronic structure and covalent bonding.

For $CeCl_6^{2-}$, the Cl K-edge XAS results and the X-ray absorption spectra collected at the Ce $L_{3,2}$- and $M_{5,4}$-edges were all internally consistent. Overall these data showed explicit evidence for substantial Ce−Cl orbital mixing. The analyses of $CeCl_6^{2-}$ at the Ce $L_{3,2}$-edge exhibited the double white line absorptions, and the Ce $M_{5,4}$-edge XAS data contained satellite features similar to those observed from CeO_2. While still heavily debated, these types of spectra have been interpreted as being diagnostic of a multiconfigurational ground state.[5,24,42,74−93] It is interesting that these types of spectra can be observed for Ce complexes containing simple Cl$^-$ ligands. However, our CI calculations conducted using CTM4XAS provided a good description of the $CeCl_6^{2-}$ $M_{5,4}$-edge data, associating it primarily with *a multiconfigurational final state*. Additional work on this interesting problem is certainly needed here.

For f-elements, understanding the roles of the frontier f- and d-orbitals has represented a longstanding challenge in both

rare-earth and actinide chemistry. For lanthanides, however, the option for covalent bonding is often dismissed, and the lanthanide−ligand interaction is regarded as being largely ionic. Here, we have provided experimental and theoretical results that indicate both the 4f- and 5d-orbitals should be considered when evaluating Ln−Cl bonding. Moreover, these results provided an opportunity to compare orbital mixing with transition metal and actinide halides that have previously been analyzed using Cl K-edge XAS. Previous Cl K-edge XAS results from octahedral MCl_6^{2-} hexahalides (M = Ti, Zr, Hf, U) are compared with the $CeCl_6^{2-}$ measurements described here in Figure 15. For the tetravalent metals, these comparisons
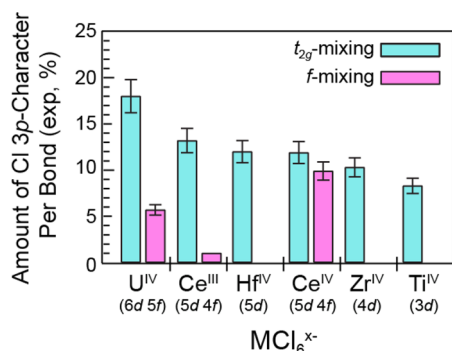
Figure 15. Comparison of the amount of Cl 3p-character per M−Cl bond (%) experimentally determined using Cl K-edge XAS for O_h-$CeCl_6^{3-}$ and O_h-$M^{IV}Cl_6^{2-}$ (M = U,[7] Ce, Hf,[7] Zr,[7] Ti[7]). For the octahedral compounds, the amount of Cl 3p-character (%) in the t_{2g} orbitals (aqua bars) and in the f-orbitals (pink bars) is shown.

showed an increase in M−Cl π-orbital mixing (t_{2g}^*) as the periodic table was descended from Ti^{IV} (3d) to Zr^{IV} (4d), then to Hf^{IV} (5d) and Ce^{IV} (5d), and ending with U^{IV} (6d). To better understand these trends, first-order perturbation theory has been considered, as described previously.[7,118,143] The theory states that orbital mixing is directly proportional to spatial overlap of the atomic orbitals and is inversely proportional to the energy difference between the two atomic orbitals. In this context, it is likely that as the quantum number increased for the metal valence orbitals (from 3d to 4d, 5d, and 6d), more d-orbital covalency resulted from improved spatial overlap of the increasingly diffuse d-orbitals.

Surprisingly, in the MCl_6^{2-} framework, we observed the 4f-orbital participation in $CeCl_6^{2-}$ to be more than twice that observed for the more diffuse 5f-orbitals in UCl_6^{2-}, as was evident from the amount of Cl 3p-character for $CeCl_6^{2-}$ vs UCl_6^{2-}, 9.9(9) vs 5.7(6)%,[7] respectively. In this case, we attributed the increase in $CeCl_6^{2-}$ 4f-orbital mixing to the lower energy of the Ce 4f- vs U 5f-orbitals. Another example where near-degeneracy seems to influence covalency in bonding to a larger extent than orbital spatial overlap is borne out by comparing the appreciable Ce 4f- and Cl 3p-orbital mixing in $CeCl_6^{2-}$ (formally Ce^{IV}) to $CeCl_6^{3-}$ (formally Ce^{III}), where 4f-orbital participation in covalent bonding was negligible. Overall, these comparisons highlight the complex interplay between orbital spatial overlap and energy near-degeneracy-driven covalency in transition metal, lanthanide, and actinide elements. Current efforts are focused on better understanding how these two variables influence orbital mixing across the periodic table and as a function of formal oxidation state. Our efforts in doing so will be heavily supported by attempts to extend this work to the transuranic actinides and comparatively evaluate how both

4f/5f- and 5d/6d-orbital mixing vary as both the lanthanide and actinide series are traversed.

■ EXPERIMENTAL SECTION

General Considerations. Except where noted, the syntheses and manipulation of all compounds reported herein were conducted under helium or argon atmospheres with rigorous exclusion of air and water by standard Schlenk, glovebox, and glovebag techniques. The $(NEt_4)_2CeCl_6$ trivalent lanthanide hexahalide salts, Z_3LnCl_6 (Ln = Nd, Sm, Eu, Gd and Z = NEt_4; Ln = Ce and Z = PPh_4), were prepared using synthetic procedures that deviated slightly from those previously reported.[69−73] Prior to XAS analyses, the hexahalide salts were crystallized and characterized by single-crystal XRD. Acetonitrile and diethyl ether (anhydrous, Aldrich) were distilled from calcium hydride or sodium/benzophenone, respectively, and degassed by three freeze−pump−thaw cycles. The D_{2d}-Cs_2CuCl_4 intensity and energy calibration standard[46,48,144−146] was prepared as previously described.[147] Single crystals were mounted in a nylon cryoloop with Paratone-N oil. Crystallographic data were collected on a Bruker D8 diffractometer, with an APEX II charge-coupled-device (CCD) detector, and cooled to 120(1) K using an American Cryoindustries low-temperature device. The instrument was equipped with graphite monochromatized Mo Kα X-ray source (λ = 0.71073 Å) and a 0.5 mm monocapillary. A hemisphere of data was collected using ω scans, with 10−30 s frame exposures and 0.5° frame widths. Data collection and initial indexing and cell refinement were handled using APEX II software.[148] Frame integration, including Lorentz-polarization corrections, and final cell parameter calculations were carried out using SAINT+ software.[149] The data were corrected for absorption using redundant reflections and the SADABS program.[150] Decay of reflection intensity was not observed as monitored via analysis of redundant frames. The structure was solved using direct methods and difference Fourier techniques. The final refinement included anisotropic temperature factors on all non-hydrogen atoms. Structure solution and refinement were performed using SHELXTL.[151]

Bis(tetraethylammonium) Cerium(IV) Hexachloride, $(NEt_4)_2CeCl_6$. In a fume hood under an atmosphere of air, an intimate mixture of NEt_4Cl (1.996 g, 12 mmol) and $Ce(SO_4)_2 \cdot xH_2O$ (2.000 g, 6 mmol) was dissolved in cold HCl_{aq} (12 M; 10 mL). Subsequently, a second aliquot of NEt_4Cl (0.020 g, 0.12 mmol) was added, and the solution was cooled to 5 °C. The yellow precipitate that formed was isolated by vacuum filtration, dried, and washed with acetone (20 mL). The solid was dissolved in hot acetonitrile. After slow cooling, single-crystals formed, and $(NEt_4)_2CeCl_6$ was isolated in 21% crystalline yield. Prior to XAS analysis, the crystals were characterized by single-crystal XRD. Diffraction. Anal. Calcd. For $C_{16}H_{40}Cl_6CeN_2$; C, 31.47; H, 6.61; N, 4.59; Cl, 34.39. Found, C, 31.52; H, 6.60; N, 4.51; Cl, 34.48.

Tris(tetraphenylphosphonium) Cerium(III) Hexachloride, $(PPh_4)_3CeCl_6$. In an argon-filled glovebox, PPh_4Cl (0.454 g, 0.12 mmol) dissolved in acetonitrile (5 mL) was added to a vial charged with $CeCl_3$ (0.100 g, 0.4 mmol) suspended in acetonitrile (10 mL). The solution was heated to 50 °C for several hours. After cooling to room temperature the solution was filtered and the volume was reduced to 10 mL in vacuo. Approximately 5 mL of diethyl ether was allowed to diffuse at room temperature and after several days single-crystals of $(PPh_4)_3CeCl_6$ were obtained in 81% crystalline yield. Prior to XAS analysis, the crystals were characterized by single-crystal XRD. Diffraction. Anal. Calcd. For $C_{72}H_{60}Cl_6CeP_3$; C, 63.20; H, 4.42; P, 6.80; Cl, 15.35. Found, C, 61.73; H, 4.57; P, 6.55; Cl, 15.11.

Tris(tetraethylammonium) Neodymium Hexachloride, $(NEt_4)_3NdCl_6$. In an argon-filled glovebox, NEt_4Cl (0.660 g, 4 mmol) dissolved in acetonitrile (5 mL) was added to a vial charged with $NdCl_3$ (0.333 g, 1.3 mmol) suspended in acetonitrile (10 mL). The solution was heated to 50 °C for several hours. After cooling to room temperature a microcrystalline solid precipitated. The supernate was removed and the solid washed with small fractions of acetonitrile. The solid was dissolved in approximately 3 mL of boiling acetonitrile and slowly cooled to room temperature. After several days single-crystals of $(NEt_4)_3NdCl_6$ were obtained in 76% crystalline yield. Prior

to XAS analysis, the crystals were characterized by single-crystal XRD. Anal. Calcd. For $C_{24}H_{60}Cl_6NdN_3$; C, 38.80; H, 8.15; N, 5.66. Found, C, 39.10; H, 8.46; N, 5.41.

Tris(tetraethylammonium) Samarium Hexachloride, $(NEt_4)_3SmCl_6$. Single crystals of $(NEt_4)_3SmCl_6$ were obtained from NEt_4Cl (0.600 g, 3.6 mmol) and $SmCl_3$ (0.313 g, 1.2 mmol) as described above for $(NEt_4)_3NdCl_6$ in 61% crystalline yield. Prior to XAS analysis, the crystals were characterized by single-crystal XRD. Anal. Calcd. For $C_{24}H_{60}Cl_6SmN_3$; C, 38.29; H, 8.04; N, 5.58. Found, C, 38.53; H, 8.27; N, 5.42.

Tris(tetraethylammonium) Europium Hexachloride, $(NEt_4)_3EuCl_6$. The $(NEt_4)_3EuCl_6$ complex was synthesized from NEt_4Cl (0.600 g, 3.6 mmol) and $EuCl_3$ (0.321 g, 1.2 mmol) in analogy to the $(NEt_4)_3NdCl_6$ synthesis described above. Single crystals were grown by allowing diethyl ether to slowly diffuse into a saturated acetonitrile solution, such that $(NEt_4)_3EuCl_6$ was obtained as single-crystals in 82% crystalline yield. Prior to XAS analysis, the crystals were characterized by single-crystal XRD. Anal. Calcd. For $C_{24}H_{60}Cl_6EuN_3$; C, 38.24; H, 8.03; N, 5.58. Found, C, 38.76; H, 8.31; N, 6.08.

Tris(tetraethylammonium) Gadolinium Hexachloride, $(NEt_4)_3GdCl_6$. Single crystals of $(NEt_4)_3GdCl_6$ were obtained from NEt_4Cl (0.600 g, 3.6 mmol) and $GdCl_3$ (0.316 g, 1.2 mmol) as described above for $(NEt_4)_3NdCl_6$. The $(NEt_4)_3GdCl_6$ salt was obtained in 93% crystalline yield. Prior to XAS analysis, the crystals were characterized by single-crystal XRD. Anal. Calcd. For $C_{24}H_{60}Cl_6GdN_3$; C, 37.98; H, 7.98; N, 5.54. Found, C, 38.33; H, 8.38; N, 5.65.

Ce $L_{3,2}$-Edge XAFS. Samples of $(PPh_4)_3CeCl_6$ and $(NEt_4)_2CeCl_6$ for the Ce $L_{3,2}$-edge X-ray measurements were prepared under an argon atmosphere. The samples were diluted with boron nitride, which was dried at elevated temperature (200 °C) under vacuum (10^{-3} Torr) for 48 h prior to use. A mixture of the analyte and BN were weighed out, such that the edge jump for the absorbing atom was calculated to be at 1 absorption length in transmission. Samples were loaded into a sample well equipped with Kapton windows. The samples were removed from the glovebox and immediately submerged into liquid N_2. These samples were analyzed in a He_{liq} cryostat at variable temperatures (100 to 6 K). The cryostat was attached to the beamline 11-2 XAFS rail (SSRL), which was equipped with three ionization chambers through which nitrogen gas was continually flowed. One chamber was positioned before the cryostat to monitor the incident radiation (I_0). The second chamber was positioned after the cryostat so that sample transmission (I_1) could be evaluated against I_0 and so that the absorption coefficient (μ) could be calculated as $\ln(I_0/I_1)$. The third chamber (I_2) was positioned downstream from I_1 so that the XANES of a calibration foil could be measured against I_1. Samples were calibrated to the energy of the first inflection point of the K-edge of a chromium foil (5989 eV), whose spectrum was measured before and after each analyte spectrum.

The X-ray absorption spectra (XAS) and extended X-ray near edge fine structure (EXAFS) were measured at the Stanford Synchrotron Radiation Lightsource (SSRL) under dedicated operating conditions (3.0 GeV, 5%, 500 mA using continuous top-off injections) on end station 11-2. This beamline, which was equipped with a 26-pole, 2.0 T wiggler, utilized a liquid nitrogen-cooled double-crystal Si[220] monochromator and employed collimating and focusing mirrors. A single energy was selected from the white beam with a liquid-N_2-cooled double-crystal monochromator utilizing Si[220] ($\varphi = 0$) crystals. Harmonic rejection was achieved by detuning the second crystal of the monochromator by 70% at 7000 eV. The horizontal and vertical slit sizes were 2.5 and 1 mm, respectively.

Ce $M_{5,4}$-Edge XAS Measurements. Samples for STXM measurements were encapsulated between two 100 nm Si_3N_4 membranes (Silson), as described previously.[60,100,152,153] Single-energy images and Ln $M_{5,4}$-edge XAS spectra were acquired using the STXM instrument at the Molecular Environmental Science Beamline 11.0.2 of the Advanced Light Source, which is operated in topoff mode at 500 mA, in a ~0.5 atm He-filled chamber.[154] Energy calibrations were performed at the Ne K-edge for Ne (867.3 eV). The energy resolution (fwhm) was estimated at 0.2 eV, and spectra were collected using

circularly polarized radiation. For these measurements, the X-ray beam was focused with a zone plate onto the sample, and the transmitted X-rays were detected. Images at a single energy were obtained by raster-scanning the sample and collecting transmitted monochromatic X-rays as a function of sample position. Spectra at each image pixel or particular regions of interest in the sample image were extracted from the "stack," which is a collection of images recorded at multiple, closely spaced photon energies across the absorption edge. Dwell times used to acquire an image at a single photon energy were ~1 ms per pixel. To quantify the absorbance signal, the measured transmitted intensity (I) was converted to optical density using the Beer–Lambert law: OD $= \ln(I/I_0) = \mu\rho d$, where I_0 is the incident photon flux intensity, d is the sample thickness, and μ and ρ are the mass absorption coefficients and density of the sample material, respectively. Incident beam intensity was measured through the sample-free region of the Si_3N_4 windows. Regions of particles with absorption of >1.5 OD were omitted to ensure the spectra were in the linear regime of the Beer–Lambert law. During the STXM experiment, particles of $CeCl_6^{3-}$ showed no sign of radiation damage and each spectrum was reproduced several times on independent particles and unique samples. Accurate and reproducible spectra of $CeCl_6^{2-}$ were obtained by averaging data obtained from a large sample area comprised of more than 50 particles, owing to radiation damage during long acquisition times on small particles. The data were fit with a first-order polynomial in the pre-edge region below the M_5-edge, then subtracted from the experimental data to eliminate the background of the spectrum. Second-derivative spectra were used as guides to determine the number and position of peaks, and the area under the M_5- and M_4-edges was determined by integration. Both of these operations were conducted using the program IGOR 6.0.

Cl K-Edge XAS Sample Preparation. Solid-state XAS samples were prepared in an argon-filled glovebox and mounted in an aluminum sample holder. The holder was an aluminum plate with 5 × 20 × 1 mm slots. Single-sided tape that had been confirmed to contain low concentrations of Cl by Cl K-edge XAS spectroscopy was fixed to the back side of the holder. The analyte was prepared by finely grinding the sample (ca. 10−20 mg) for 2 min in polystyrene canisters with Plexiglas pestles using a Wig-L-Bug grinder to obtain a homogeneous fine powder. Samples were painted onto the single-sided tape using paintbrushes. The sample holder was sealed by adhering a 4 μm polypropylene window to the front side of the sample holder with double-sided tape. All samples were sealed in Mylar bags, removed from the glovebox, and shipped. Once unpackaged, the samples were immediately attached to the sample translator and inserted into a sample chamber flushed with He gas.

Cl K-Edge XAS Measurements. All Cl K-edge XAS data were either collected at the beamlines 6-2 (SSRL), 4-3 (SSRL), or the INE beamline for Actinide Research at ANKA. The Cl K-edge XAS measurements made at SSRL were conducted under dedicated operating conditions (3.0 GeV, 500 mA) at beamline 4-3. This beamline was equipped with a 20-pole, 2.0 T wiggler, utilized a liquid-N_2-cooled double-crystal Si[111] monochromator and employed flat, bent vertically collimating and focusing mirrors (fwhm beam spot size =3 × 16 mm). At ANKA, operating conditions of 2.5 GeV and 120 mA were used. The beamline was equipped with a 1.5 T bending magnet and a water-cooled Si[111] double-crystal monochromator. The crystals were detuned by 30% from the rocking curve maximum.[155] Two mirrors were utilized, the first mirror vertically collimating and the second mirror vertically and horizontally focusing.

At both facilities, samples were analyzed within a chamber that was separated from the beam pipe by a 4 μm polypropylene window and continually flushed with He gas. An additional window of the same material separated the sample from a Vortex Si fluorescence detector (4-element, SSRL; 1-element, ANKA) that was positioned at 90° from the incident beam and sufficiently far from the sample to ensure dead times that were less than 3%. Sample fluorescence was measured using the Vortex detector against the incident radiation (I0), which was monitored using an ionization chamber through which He was continually flowed. The ion chamber was isolated from the sample chamber with a 4 μm polypropylene window. Spectra were collected with dwell times of 1−3 s. Dead time corrections to all experimental

scans collected at SSRL were achieved by measuring fluorescence intensities of the Vortex elements vs the total counts and opening the horizontal slit (starting at 0.1 mm slit width) in steps of 0.1 mm until full saturation was achieved. Detector dead times were evaluated by obtaining a response curve for the single channel analyzer (SCA) vs the incoming count rate (ICR) of the detector. The SCA-to-ICR relationship was modeled assuming that $r = kr_1 e^{-rt}$, where t is the dead time, r is the SCA count rate, r_1 is the ICR count rate, and k is a proportionality constant. These analyses showed dead time contributions of less than 3%.

Cl K-Edge XAS Data Analysis. Data manipulation and analysis was conducted as previously described by Solomon and co-workers.[48] Energy calibrations were conducted externally using the maxima of the first pre-edge features in Cs_2CuCl_4 (2820.02 eV).[48] Data were analyzed by fitting a line to the pre-edge region, 2702.1−2815.0 eV, which was subsequently subtracted from the experimental data to eliminate the background of the spectrum. The data were normalized by fitting a first-order polynomial to the post-edge region of the spectrum (2836−3030 eV) and setting the edge jump at 2836 eV to an intensity of 1.0. This normalization procedure gave spectra normalized to a single Cl atom or M−Cl bond. A deconvoluted model for the Cl K-edge XAS data was obtained using a modified version of EDG_FIT[156] in IGOR 6.0. The pre-edge regions (<2824.8 eV) were best modeled by two symmetry-constrained pseudo-Voigt line shapes. Approximate peak positions were determined using first and second derivatives of each spectrum. The edge regions were modeled with two pseudo-Voigt functions (for the edge peak) and an additional function consisting of a 1:1 ratio of arctangent and error function contributions, which was used to model the absorption threshold. Deconvoluted spectral models were performed over several energy ranges. To facilitate comparison with previously reported Cl K-edge XAS spectra for $(PPh_4)_2MCl_6$ (M = Ti, Zr, Hf, U),[7] the energy position for the step function was optimized near the value used previously. The areas under the pre-edge peaks (hereafter defined as the intensity) are equal to the fwhm × peak height. Spectra were obtained in triplicate, with unique samples of the lanthanide hexahalides being analyzed during four different synchrotron scheduling periods to establish reproducibility and evaluate error associated with the measurements.

Ground-State DFT Calculations. Ground-state electronic structure calculations were performed on the $LnCl_6^{3-}$ (Ln = Ce, Pr, Nd, Pm, Sm, Eu, Gd) and $CeCl_6^{2-}$ complexes using B3LYP hybrid DFT)[157,158] in the Gaussian 09 code.[159] For all $LnCl_6^{3-}$ complexes, an unrestricted calculation was employed. In this case the two density matrices can differ because the SCF is carried out separately for the α and β spins, which can result in different orbitals for α and β (referred to as α and β spin−orbitals). The Stuttgart 97 RECP and associated basis sets (without the most diffuse function) were used for all metals.[160−162] Chlorine was modeled using a Pople style double-ζ 6-31G(d′) basis set with polarization functions optimized for heavy atoms.[163,164] Spin−orbit interactions were not included in the calculations. These functionals and basis sets have been extensively tested for organometallic and inorganic systems and shown to give good agreement with experimental data.[6−8,57−60,66−68,133−135] The populations for the Cl 3p-orbitals were then obtained by Mulliken population analyses in each orbital. For comparison with experimental values, calculated values of the % Cl 3p-character in each orbital were normalized to per-bond values by multiplying the total Cl 3p-character by the sum of the squares of the normalization constants for the corresponding ligand−orbital wave functions. For example, the 3.9% Cl 3p-character found in the triply degenerate set of t_{2g} orbitals for $CeCl_6^{2-}$ was corrected by $(1/2)^2 + (1/2)^2 + (1/2)^2 = 3/4$ in accordance with the mathematical representation for the d_{xy}, d_{xz}, and d_{yz} metal orbitals, which are $^1/_2(x_1 + y_2 + y_3 + x_4)$, $^1/_2(y_1 + x_5 + x_3 + y_6)$, and $^1/_2(x_2 + y_5 + y_4 + x_6)$, respectively.[7,66] Where a given orbital was found to have both σ- and π-bonding character (e.g., the t_{1u} 5f-orbitals), the σ- and π-bonding components were normalized independently first and then summed together to provide the calculated per-bond values in Tables 1 and 2.

CTM4XAS Multiplet Calculations. Multiplet calculations were implemented using CTM4XAS, which is a program based on the original code by Cowan[111] and further developed by de Groot.[112,113] Effects of the crystal field are typically minimal in f-sytems, so they were not included.[111] For Ce^{III}, the graphical user interface was implemented with F_{ff} at 79%, SOC at 98%, and F_{df} and G_{df} at 100% of atomic values. A Gaussian broadening of 0.25 eV was applied to account for instrumental broadening and Lorentzian broadenings of 0.2 and 0.4 eV were applied to the M_5- and M_4-edges, respectively.

Charge transfer for f-block systems is not implemented in the GUI interface of the program, so all calculations for Ce^{IV} were run from the command line (sample input files may be found in the Supporting Information). For Ce^{IV}, F_{ff} was left at atomic values, F_{fd} reduced to 40%, SOC reduced to 99%, and G_{fd} reduced to 80% of atomic values. For the $3d^9 4f^1$ configuration, these reductions result in values of F_{fd} = 2.622 eV, SOC = 7.293 eV, and G_{fd} = 3.621 eV. Δ_{IS} was set to 2.5 eV, Δ_{FS} = −1.5 eV, and $T_{IS} = T_{FS}$ = 0.7 eV. For the $3d^9 \underline{L} 4f^2$ configuration, these reductions result in values of F_{ff} = 10.102 eV, F_{fd} = 2.396 eV, SOC = 7.297 eV, and G_{fd} = 3.247 eV. Δ_{IS} was set to 2.5 eV, Δ_{FS} = −1.5 eV, and $T_{IS} = T_{FS}$ = 0.7 eV. A Gaussian broadening of 0.25 eV was applied to account for instrumental broadening and Lorentzian broadenings of 0.4 and 0.6 eV were applied to the M_5- and M_4-edges, respectively.

TDDFT Calculations. For the $LnCl_6^{3-}$ and $CeCl_6^{2-}$ anions, the Cl K-edge XAS spectra were simulated using TDDFT calculations, which were conducted as previously described.[6−8,57−60,66−68,133−135] Specifically, this analysis involved a linear response calculation for extracting the transition amplitudes from the transition densities and dipole moments between the calculated excited states and the ground-states. The excitations originating from all of the intermediate states between the Cl 1s-orbitals and the highest occupied molecular orbital were excluded so that only excitations from the core levels to virtual orbitals could be analyzed. This allowed the virtual orbitals to relax under the influence of the Cl core−hole, but not the occupied orbitals. Although excluding relaxations in the occupied space resulted in large errors associated with absolute calculated transition energies, the relative energies addressed the first-order changes in virtual orbitals accompanying the core−hole excitation. As discussed previously,[137,138] an energy shift was established to account for the omission of the atomic and extra-atomic relaxation associated with the core excitation, relativistic stabilization, and errors associated with the functional. This was achieved by setting the energy of transitions simulated for the 6d-orbitals to be equal to those in the experimental spectra, which resulted in an energy shift of +64 eV for all simulated spectra of all treated compounds, respectively.

■ ASSOCIATED CONTENT

Ⓢ Supporting Information

Background-subtracted and normalized X-ray absorption data and analyses, complete ref 159, XRD data for the $LnCl_6^{3-}$ compounds, and CTM4XAS sample input files. This material is available free of charge via the Internet at http://pubs.acs.org. The structures for the $LnCl_6^{3-}$ compounds were additionally submitted to the Cambridge Structural Database (CCDC Nos. 1021660−1021664).

■ AUTHOR INFORMATION

Corresponding Authors
*erb@lanl.gov
*stosh@lanl.gov
*rlmartin@lanl.gov

Notes

The authors declare no competing financial interest.

■ ACKNOWLEDGMENTS

■ REFERENCES

(1) Heitler, W.; London, F. Z. *Phys.* **1927**, *44*, 455.
(2) Kaltsoyannis, N.; *The f-Elements*; Oxford University Press: Oxford, 1999.
(3) Burns, C. J.; Bursten, B. E. *Comments Inorg. Chem.* **1989**, *9*, 61.
(4) Clark, D. L.; Gordon, J. C.; Hay, P. J.; Poli, R. *Organometallics* **2005**, *24*, 5747.
(5) Kerridge, A. *Dalton Trans.* **2013**, *42*, 16428.
(6) Kozimor, S. A.; Yang, P.; Batista, E. R.; Boland, K. S.; Burns, C. J.; Clark, D. L.; Conradson, S. D.; Martin, R. L.; Wilkerson, M. P.; Wolfsberg, L. E. *J. Am. Chem. Soc.* **2009**, *131*, 12125.
(7) Minasian, S. G.; Keith, J. M.; Batista, E. R.; Boland, K. S.; Clark, D. L.; Conradson, S. D.; Kozimor, S. A.; Martin, R. L.; Schwarz, D. E.; Shuh, D. K.; Wagner, G. L.; Wilkerson, M. P.; Wolfsberg, L. E.; Yang, P. *J. Am. Chem. Soc.* **2012**, *134*, 5586.
(8) Minasian, S. G.; Keith, J. M.; Batista, E. R.; Boland, K. S. *Chem. Sci.* **2014**, *5*, 351.
(9) Raymond, K. N.; Eigenbrot, C. W. *Acc. Chem. Res.* **1980**, *13*, 276.
(10) Jensen, M. P.; Bond, A. H. *J. Am. Chem. Soc.* **2002**, *124*, 9870.
(11) Evans, W. J.; Kozimor, S. A.; Nyce, G. W.; Ziller, J. W. *J. Am. Chem. Soc.* **2003**, *125*, 13831.
(12) Cotton, S. *Lanthanide and Actinide Chemistry*, 1st ed.; John Wiley & Sons Ltd.: Chichester, 2006.

(13) Crosswhite, H. M.; Crosswhite, H.; Carnall, W. T.; Paszek, A. P. *J. Chem. Phys.* **1980**, *72*, 5103.
(14) Cundari, T. R.; Stevens, W. J. *J. Chem. Phys.* **1993**, *98*, 5555.
(15) Hong, G.; Schautz, F.; Dolg, M. *J. Am. Chem. Soc.* **1999**, *121*, 1502.
(16) Maron, L.; Eisenstein, O. *J. Phys. Chem. A* **2000**, *104*, 7140.
(17) Vetere, V.; Maldivi, P.; Adamo, C. *J. Comput. Chem.* **2003**, *24*, 850.
(18) Atanasov, M.; Daul, C.; Güdel, H. U.; Wesolowski, T. A.; Zbiri, M. *Inorg. Chem.* **2005**, *44*, 2954.
(19) Bünzli, J.-C. G.; Eliseeva, S. V. In *Lanthanide Luminescence*; Springer Series on Fluorescence; Springer Berlin Heidelberg: Berlin, Heidelberg, 2010; Vol. 7, pp 1−45.
(20) Li, Q.-P.; Yan, B. *Photochem. Photobiol.* **2013**, *90*, 22.
(21) Bünzli, J.-C. G.; Piguet, C. *Chem. Soc. Rev.* **2005**, *34*, 1048.
(22) Mares, F.; Hodgson, K. O.; Streitwieser, A., Jr. *J. Organomet. Chem.* **1970**, *24*, C68.
(23) Greco, A.; Cesca, S.; Bertolini, G. *J. Org. Chem.* **1976**, *113*, 321.
(24) Dexpert, H.; Karnatak, R.; Esteva, J.; Connerade, J.; Gasgnier, M.; Caro, P.; Albert, L. *Phys. Rev. B* **1987**, *36*, 1750.
(25) Selg, P.; Brintzinger, H. H.; Schultz, M.; Andersen, R. A. *Organometallics* **2002**, *21*, 3100.
(26) Anderson, D. M.; Cloke, F. G. N.; Cox, P. A.; Edelstein, N.; Green, J. C.; Pang, T.; Sameh, A. A.; Shalimoff, G. *J. Chem. Soc., Chem. Commun.* **1989**, 53.
(27) King, W. A.; Marks, T. J.; Anderson, D. M.; Duncalf, D. J.; Cloke, F. G. N. *J. Am. Chem. Soc.* **1992**, *114*, 9221.
(28) Gordon, J. C.; Giesbrecht, G. R.; Clark, D. L.; Hay, P. J.; Keogh, D. W.; Poli, R.; Scott, B. L.; Watkin, J. G. *Organometallics* **2002**, *21*, 4726.
(29) Giesbrecht, G. R.; Gordon, J. C.; Clark, D. L.; Hay, P. J.; Scott, B. L.; Tait, C. D. *J. Am. Chem. Soc.* **2004**, *126*, 6387.
(30) Evans, W. J.; Lee, D. S. *Can. J. Chem.* **2005**, *83*, 375.
(31) Arnold, P. L.; Turner, Z. R.; Kaltsoyannis, N.; Pelekanaki, P.; Bellabarba, R. M.; Tooze, R. P. *Chem.—Eur. J.* **2010**, *16*, 9623.
(32) Huang, W.; Khan, S. I.; Diaconescu, P. L. *J. Am. Chem. Soc.* **2011**, *133*, 10410.
(33) Gong, Y.; Wang, X.; Andrews, L.; Chen, M.; Dixon, D. A. *Organometallics* **2011**, *30*, 4443.
(34) Krinsky, J. L.; Minasian, S. G.; Arnold, J. *Inorg. Chem.* **2011**, *50*, 345.
(35) Lukens, W. W.; Magnani, N.; Booth, C. H. *Inorg. Chem.* **2012**, *51*, 10105.
(36) Nocton, G.; Lukens, W. W.; Booth, C. H.; Rozenel, S. S.; Medling, S. A.; Maron, L.; Andersen, R. A. *J. Am. Chem. Soc.* **2014**, *136*, 8626.
(37) Robinson, J. R.; Gordon, Z.; Booth, C. H.; Carroll, P. J.; Walsh, P. J.; Schelter, E. J. *J. Am. Chem. Soc.* **2013**, *135*, 19016.
(38) Bogart, J. A.; Lewis, A. J.; Medling, S. A.; Piro, N. A.; Carroll, P. J.; Booth, C. H.; Schelter, E. J. *Inorg. Chem.* **2013**, *52*, 11600.
(39) Hazin, P. N.; Bruno, J. W.; Brittain, H. G. *Organometallics* **1987**, *6*, 913.
(40) Kaltsoyannis, N.; Bursten, B. E. *J. Organomet. Chem.* **1997**, *528*, 19.
(41) Sekiya, M.; Noro, T.; Miyoshi, E.; Osanai, Y.; Koga, T. *J. Comput. Chem.* **2006**, *27*, 463.
(42) Mooßen, O.; Dolg, M. *Chem. Phys. Lett.* **2014**, *594*, 47.
(43) Humphries, M. *Rare Earth Elements: The Global Supply Chain*; Congressional Research Service: Washington, DC, Dec 16, 2013; p R41347.
(44) Hedman, B.; Hodgson, K. O.; Solomon, E. I. *J. Am. Chem. Soc.* **1990**, *112*, 1643.
(45) Shadle, S. E.; Penner-Hahn, J. E.; Schugar, H. J.; Hedman, B.; Hodgson, K. O.; Solomon, E. I. *J. Am. Chem. Soc.* **1993**, *115*, 767.
(46) Shadle, S. E.; Hedman, B.; Hodgson, K. O.; Solomon, E. I. *J. Am. Chem. Soc.* **1995**, *117*, 2259.
(47) Glaser, T.; Hedman, B.; Hodgson, K. O.; Solomon, E. I. *Acc. Chem. Res.* **2000**, *33*, 859.

(48) Solomon, E. I.; Hedman, B.; Hodgson, K. O.; Dey, A.; Szilagyi, R. K. *Coord. Chem. Rev.* **2005**, *249*, 97.

(49) DeBeer George, S.; Brant, P.; Solomon, E. I. *J. Am. Chem. Soc.* **2005**, *127*, 667.

(50) Kozimor, S. A.; Yang, P.; Batista, E. R.; Boland, K. S.; Burns, C. J.; Christensen, C. N.; Clark, D. L.; Conradson, S. D.; Hay, P. J.; Lezama, J. S.; Martin, R. L.; Schwarz, D. E.; Wilkerson, M. P.; Wolfsberg, L. E. *Inorg. Chem.* **2008**, *47*, 5365.

(51) Sarangi, R.; Yang, L.; Winikoff, S. G.; Gagliardi, L.; Cramer, C. J.; Tolman, W. B.; Solomon, E. I. *J. Am. Chem. Soc.* **2011**, *133*, 17180.

(52) Sproules, S.; Weyhermüller, T.; Goddard, R.; Wieghardt, K. *Inorg. Chem.* **2011**, *50*, 12623.

(53) Liu, L.; Burnyeat, C. A.; Lepsenyi, R. S.; Nwabuko, I. O.; Kelly, T. L. *Chem. Mater.* **2013**, *25*, 4206.

(54) Queen, M. S.; Towey, B. D.; Murray, K. A.; Veldkamp, B. S.; Byker, H. J.; Szilagyi, R. K. *Coord. Chem. Rev.* **2013**, *257*, 564.

(55) Donahue, C. M.; Pacheco, J. S. L.; Keith, J. M.; Daly, S. R. *Dalton Trans.* **2014**, *43*, 9189.

(56) Silver, S. C.; Gardenghi, D. J.; Naik, S. G.; Shepard, E. M.; Huynh, B. H.; Szilagyi, R. K.; Broderick, J. B. *J. Biol. Inorg. Chem.* **2014**, *19*, 465.

(57) Casarin, M.; Finetti, P.; Vittadini, A.; Wang, F.; Ziegler, T. *J. Phys. Chem. A* **2007**, *111*, 5270.

(58) DeBeer George, S.; Neese, F. *Inorg. Chem.* **2010**, *49*, 1849.

(59) DeBeer George, S.; Petrenko, T.; Neese, F. *Inorg. Chim. Acta* **2008**, *361*, 965.

(60) Minasian, S. G.; Keith, J. M.; Batista, E. R.; Boland, K. S.; Kozimor, S. A.; Martin, R. L.; Shuh, D. K.; Tyliszczak, T.; Vernon, L. J. *J. Am. Chem. Soc.* **2013**, *135*, 14731.

(61) Szilagyi, R. K.; Bryngelson, P. A.; Maroney, M. J.; Hedman, B.; Hodgson, K. O.; Solomon, E. I. *J. Am. Chem. Soc.* **2004**, *126*, 3018.

(62) DeBeer George, S.; Huang, K.-W.; Waymouth, R. M.; Solomon, E. I. *Inorg. Chem.* **2006**, *45*, 4468.

(63) Bradley, J. A.; Yang, P.; Batista, E. R.; Boland, K. S.; Burns, C. J.; Clark, D. L.; Conradson, S. D.; Kozimor, S. A.; Martin, R. L.; Seidler, G. T.; Scott, B. L.; Shuh, D. K.; Tyliszczak, T.; Wilkerson, M. P.; Wolfsberg, L. E. *J. Am. Chem. Soc.* **2010**, *132*, 13914.

(64) Tenderholt, A. L.; Wang, J.-J.; Szilagyi, R. K.; Holm, R. H.; Hodgson, K. O.; Hedman, B.; Solomon, E. I. *J. Am. Chem. Soc.* **2010**, *132*, 8359.

(65) Daly, S. R.; Keith, J. M.; Batista, E. R.; Boland, K. S.; Clark, D. L.; Kozimor, S. A.; Martin, R. L. *J. Am. Chem. Soc.* **2012**, *134*, 14408.

(66) Spencer, L. P.; Minasian, S. G.; Jilek, R. E.; Batista, E. R.; Boland, K. S.; Boncella, J. M.; Conradson, S. D.; Clark, D. L.; Gdula, R. L.; Hayton, T. W.; Kozimor, S. A.; Martin, R. L.; MacInnes, M. A.; Olson, A. C.; Scott, B. L.; Shuh, D. K.; Yang, P. *J. Am. Chem. Soc.* **2013**, *135*, 1864.

(67) Wen, X.-D.; Löble, M. W.; Batista, E. R.; Bauer, E.; Boland, K. S.; Burrell, A. K.; Conradson, S. D.; Daly, S. R.; Kozimor, S. A.; Minasian, S. G.; Martin, R. L.; McCleskey, T. M.; Scott, B. L.; Shuh, D. K.; Tyliszczak, T. *J. Electron Spectrosc. Relat. Phenom.* **2014**, *194*, 81–87.

(68) Bradley, J. A.; Sen Gupta, S.; Seidler, G. T.; Moore, K. T.; Haverkort, M. W.; Sawatzky, G. A.; Conradson, S. D.; Clark, D. L.; Kozimor, S. A.; Boland, K. S. *Phys. Rev. B* **2010**, *81*, 193104.

(69) Kiselev, Y. M.; Brandt, A.; Martynenko, L. I.; Spitsyn, V. I. *Dokl. Akad. Nauk SSSR* **1979**, *246*, 879.

(70) Rogers, R. D.; Rollins, A. N.; Henry, R. F.; Murdoch, J. S.; Etzenhouser, R. D.; Huggins, S. E.; Nunez, L. *Inorg. Chem.* **1991**, *30*, 4946.

(71) Diamantopoulou, E.; Papaefstathiou, G. S.; Terzis, A.; Raptopoulou, C. P.; Desseyn, H. O.; Perlepes, S. P. *Polyhedron* **2003**, *22*, 825.

(72) Clegg, W.; Harrington, R. W. *Acta Crystallograph., Sect. E* **2007**, *63*, m1152.

(73) Hines, C. C.; Cordes, D. B.; Griffin, S. T.; Watts, S. I.; Cocalia, V. A.; Rogers, R. D. *New J. Chem.* **2008**, *32*, 872.

(74) Krill, G.; Kappler, J. P.; Meyer, A.; Abadli, L.; Ravet, M. F. *J. Phys. F* **1981**, *11*, 1713.

(75) Bianconi, A.; Marcelli, A.; Tomellini, M.; Davoli, I. *J. Magn. Magn. Mater.* **1985**, *47-48*, 209.

(76) Bianconi, A.; Marcelli, A.; Dexpert, H.; Kotani, A.; Jo, T.; Petiau, J. *Phys. Rev. B* **1987**, *35*, 806.

(77) Jo, T.; Kotani, A. *Solid State Commun.* **1985**, *54*, 451.

(78) Kaindl, G.; Wertheim, G. K.; Schmiester, G. *Phys. Rev.* **1987**, *58*, 606.

(79) Kotani, A.; Okada, K.; Okada, M. *Solid State Commun.* **1987**, *64*, 1479.

(80) Kaindl, G.; Schmiester, G.; Sampathkumaran, E.; Wachter, P. *Phys. Rev. B* **1988**, *38*, 10174.

(81) Kotani, A.; Ogasawara, H. *J. Electron Spectrosc. Relat. Phenom.* **1992**, *60*, 257.

(82) Edelstein, N. M.; Allen, P. G.; Bucher, J. J.; Shuh, D. K.; Sofield, C. D.; Kaltsoyannis, N.; Maunder, G. H.; Russo, M. R.; Sella, A. *J. Am. Chem. Soc.* **1996**, *118*, 13115.

(83) Booth, C. H.; Walter, M. D.; Daniel, M.; Lukens, W. W.; Andersen, R. A. *Phys. Rev. Lett.* **2005**, *95*, 267202.

(84) Sham, T. K.; Gordon, R. A.; Heald, S. M. *Phys. Rev. B* **2005**, *72*, 035113.

(85) Shahin, A. M.; Grandjean, F.; Long, G. J.; Schuman, T. P. *Chem. Mater.* **2005**, *17*, 315.

(86) Walter, M. D.; Booth, C. H.; Lukens, W. W.; Andersen, R. A. *Organometallics* **2009**, *28*, 698.

(87) Todorova, T. K.; Infante, I.; Gagliardi, L.; Dyke, J. M. *Int. J. Quantum Chem.* **2009**, *109*, 2068.

(88) Gaigalas, G.; Gaidamauskas, E.; Rudzikas, Z.; Magnani, N.; Caciuffo, R. *Phys. Rev. A* **2009**, *79*, 022511.

(89) Kerridge, A.; Kaltsoyannis, N. *C. R. Chim.* **2010**, *13*, 853.

(90) Kotani, A.; Kvashnina, K. O.; Butorin, S. M.; Glatzel, P. *J. Electron Spectrosc. Relat. Phenom.* **2011**, *184*, 210.

(91) Kvashnina, K. O.; Butorin, S. M.; Glatzel, P. *J. Anal. At. Spectrom.* **2011**, *26*, 1265.

(92) Liu, L.; Sham, T.-K.; Hayashi, H.; Kanai, N.; Takehara, Y.; Kawamura, N.; Mizumaki, M.; Gordon, R. A. *J. Chem. Phys.* **2012**, *136*, 194501.

(93) Kotani, A. *Mod. Phys. Lett. B* **2013**, *27*, 1330012.

(94) Fuggle, J. C.; Hillebrecht, F. U.; Esteva, J. M.; Karnatak, R. C.; Gunnarsson, O.; Schönhammer, K. *Phys. Rev. B* **1983**, *27*, 4637.

(95) Bradley, J. A.; Moore, K. T.; Lipp, M. J.; Mattern, B. A.; Pacold, J. I.; Seidler, G. T.; Chow, P.; Rod, E.; Xiao, Y.; Evans, W. J. *Phys. Rev. B* **2012**, *85*, 10980121.

(96) Hu, Z.; Cho, E. J.; Kaindl, G.; Muller, B. G. *Phys. Rev. B* **1995**, *51*, 7514.

(97) Hu, Z. W.; Kaindl, G.; Muller, B. G. *J. Alloys Compd.* **1997**, *246*, 177.

(98) Hu, Z. W.; Kaindl, G.; Meyer, G. *J. Alloys Compd.* **1997**, *246*, 186.

(99) Lee, C. H.; Oyanagi, H.; Sekine, C.; Shirotani, I.; Ishii, M. *Phys. Rev. B* **1999**, *60*, 13253.

(100) Bugaris, D. E.; Copping, R.; Tyliszczak, T.; Shuh, D. K.; Ibers, J. A. *Inorg. Chem.* **2010**, *49*, 2568.

(101) Gordon, R. A.; Seidler, G. T.; Fister, T. T.; Nagle, K. P. *J. Electron Spectrosc. Relat. Phenom.* **2011**, *184*, 220.

(102) Richter, J. H.; Ruck, B. J.; Simpson, M.; Natali, F.; Plank, N. O. V.; Azeem, M.; Trodahl, H. J.; Preston, A. R. H.; Chen, B.; McNulty, J.; Smith, K. E.; Tadich, A.; Cowie, B.; Svane, A.; van Schilfgaarde, M.; Lambrecht, W. R. L. *Phys. Rev. B* **2011**, *84*, 235120.

(103) Bradley, J. A.; Moore, K. T.; van der Laan, G.; Bradley, J. P.; Gordon, R. A. *Phys. Rev. B* **2011**, *84*, 205105.

(104) Kaindl, G.; Brewer, W. D.; Kalkowski, G.; Holtzberg, F. *Phys. Rev. Lett.* **1983**, *51*, 2056.

(105) Manoubi, T.; Colliex, C.; Rez, P. *J. Electron Spectrosc. Relat. Phenom.* **1990**, *50*, 1.

(106) Thole, B. T.; Van Der Laan, G.; Fuggle, J. C.; Sawatzky, G. A.; Karnatak, R. C.; Esteva, J. M. *Phys. Rev. B* **1985**, *32*, 5107.

(107) (a) Kaindl, G.; Kalkowski, G.; Brewer, W. D.; Perscheid, B.; Holtzberg, F. *J. Appl. Phys.* **1984**, *55*, 1910. (b) Jo, T.; Kotani, A. *Phys. Rev. B* **1988**, *38*, 830.

(108) Ayala, P.; Kitaura, R.; Nakanishi, R.; Shiozawa, H.; Ogawa, D.; Hoffmann, P.; Shinohara, H.; Pichler, T. *Phys. Rev. B* **2011**, *83*, 085407.

(109) Nakamura, T.; Hirono, T.; Kinoshita, T.; Narumi, Y.; Hayashi, M.; Nojiri, H.; Mitsuda, A.; Wada, H.; Kodama, K.; Kindo, K.; Kotani, A. *J. Phys. Soc. Jpn.* **2012**, *81*, 103705.

(110) Meihaus, K. R.; Minasian, S. G.; Lukens, W. W.; Kozimor, S. A.; Shuh, D. K.; Tyliszczak, T.; Long, J. R. *J. Am. Chem. Soc.* **2014**, *136*, 6056.

(111) Cowan, R. D. *The Theory of Atomic Structure and Spectra*; University of California Press: 1981.

(112) Stavitski, E.; de Groot, F. M. F. *Micron* **2010**, *41*, 687.

(113) de Groot, F. M. F.; Kotani, A. *Core Level Spectroscopy of Solids*; Taylor and Francis: New York, 2008.

(114) Moore, K. T.; van der Laan, G.; Haire, R. G.; Wall, M. A.; Schwartz, A. J. *Phys. Rev. B* **2006**, *73*, 003109.

(115) Fortner, J. A.; Buck, E. C. *Appl. Phys. Lett.* **1996**, *68*, 3817.

(116) Stavitski, E.; de Groot, F. M. F. *Micron* **2010**, *41*, 687.

(117) Kucheyev, S. O.; Clapsaddle, B. J.; Wang, Y. M. Y. M.; van Buuren, T.; Hamza, A. V. *Phys. Rev. B* **2007**, *76*, 235420.

(118) van Buuren, T.; Hamza, A. V. *Phys. Rev. B* **2007**, *76*, 235420.

(119) Turner, S.; Lazar, S.; Freitag, B.; Egoavil, R.; Verbeeck, J.; Put, S.; Strauven, Y.; Van Tendeloo, G. *Nanoscale* **2011**, *3*, 3385.

(120) Kucheyev, S. O.; Clapsaddle, B. J.; Wang, Y. M.; van Buuren, T.; Hamza, A. V. *Phys. Rev. B* **2007**, *76*, 235420.

(121) Turner, S.; Lazar, S.; Freitag, B.; Egoavil, R.; Verbeeck, J.; Put, S.; Strauven, Y.; Van Tendeloo, G. *Nanoscale* **2011**, *3*, 3385.

(122) de Groot, F. M. F. *Coord. Chem. Rev.* **2005**, *249*, 31.

(123) Pan, Y.; Hussey, C. L. *Inorg. Chem.* **2013**, *52*, 3241.

(124) Amberger, H. D.; Rosenbauer, G. G.; Fischer, R. D. *J. Phys. Chem. Solids* **1977**, *38*, 379.

(125) Becker, A.; Urland, W. *J. Alloys Compd.* **1998**, *275–277*, 62.

(126) Ruipérez, F.; Barandiarán, Z.; Seijo, L. *J. Chem. Phys.* **2005**, *123*, 00219606.

(127) Ballhausen, C. J.; Gray, H. B. *Molecular Orbital Theory*; W.A. Benjamin, Inc.: New York, 1965.

(128) Harris, D. C.; Bertolucci, M. D. *Symmetry and Spectroscopy. An Introduction to Vibrational and Electronic Spectroscopy*; Dover Publications, Inc.: New York, 1978.

(129) Albright, T. A.; Burdett, J. K.; Whangbo, M. H. *Orbital Interactions in Chemistry*; John Wiley and Sons: New York, 1985.

(130) Lever, A. B. P. *Inorganic Electronic Spectroscopy*, 2nd ed.; Elsevier Science: Oxford, 1985.

(131) Figgis, B. N.; Hitchman, M. A. *Ligand field theory and its applications*, 1st ed.; Wiley-VCH: Weinheim, 2000.

(132) Cotton, F. A. *Chemical Applications of Group Theory*; John Wiley & Sons: New York, 2004.

(133) Fronzoni, G.; Stener, M.; Reduce, A.; Decleva, P. *J. Phys. Chem. A* **2004**, *108*, 8467.

(134) DeBeer George, S.; Petrenko, T.; Neese, F. *J. Phys. Chem. A* **2008**, *112*, 12936.

(135) Stieber, S. C. E.; Milsmann, C.; Hoyt, J. M.; Turner, Z. R.; Finkelstein, K. D.; Wieghardt, K.; DeBeer, S.; Chirik, P. J. *Inorg. Chem.* **2012**, *51*, 3770.

(136) Wen, X.-D.; Martin, R. L.; Roy, L. E.; Scuseria, G. E.; Rudin, S. P.; Batista, E. R.; McCleskey, T. M.; Scott, B. L.; Bauer, E.; Joyce, J. J.; Durakiewicz, T. *J. Chem. Phys.* **2012**, *137*, 154707.

(137) Martin, R. L.; Shirley, D. A. Many electron theory of electron emission. In *Electron Spectroscopy: Theory, Techniques and Applications*; Brundle, C. R., Baker, A. D., Eds.; Academic Press: London, 1977; Vol. 1, pp 75–117.

(138) Segala, M.; Chong, D. P. *J. Electron Spectrosc. Relat. Phenom.* **2010**, *182*, 141.

(139) Slater, J. C. *Phys. Rev.* **1930**, *1*, 75.

(140) Westre, T. E.; Kennepohl, P.; DeWitt, J. G.; Hedman, B.; Hodgson, K. O.; Solomon, E. I. *J. Am. Chem. Soc.* **1997**, *119*, 6297.

(141) Lukens, W. W.; Edelstein, N. M.; Magnani, N.; Hayton, T. W.; Fortier, S.; Seaman, L. A. *J. Am. Chem. Soc.* **2013**, *135*, 10742.

(142) Martin, R. L. *Phys. Rev. B* **1996**, *54*, R9647.

(143) Neidig, M. L.; Clark, D. L.; Martin, R. L. *Coord. Chem. Rev.* **2013**, *257*, 394.

(144) Neese, F.; Hedman, B.; Hodgson, K. O.; Solomon, E. I. *Inorg. Chem.* **1999**, *38*, 4854.

(145) Didziulis, S. V.; Cohen, S. L.; Gewirth, A. A.; Solomon, E. I. *J. Am. Chem. Soc.* **1988**, *110*, 250.

(146) Gewirth, A. A.; Cohen, S. L.; Schugar, H. J.; Solomon, E. I. *Inorg. Chem.* **1987**, *27*, 1133.

(147) Helmholz, L.; Kruh, R. F. *J. Am. Chem. Soc.* **1952**, *74*, 1176.

(148) *APEX II 1.08*; Bruker AXS, Inc.: Madison, WI.

(149) *SAINT+ 7.06*; Bruker AXS, Inc.: Madison, WI.

(150) Sheldrick, G. *SADABS 2.03*; University of Göttingen: Göttingen, Germany.

(151) *SHELXTL 6.14*; Bruker AXS, Inc.: Madison, WI.

(152) Gianetti, T. L.; Nocton, G.; Minasian, S. G.; Tomson, N. C.; Kilcoyne, A. L. D.; Kozimor, S. A.; Shuh, D. K.; Tyliszczak, T.; Bergman, R. G.; Arnold, J. *J. Am. Chem. Soc.* **2013**, *135*, 3224.

(153) Minasian, S. G.; Krinsky, J. L.; Rinehart, J. D.; Copping, R.; Tyliszczak, T.; Janousch, M.; Shuh, D. K.; Arnold, J. *J. Am. Chem. Soc.* **2009**, *131*, 13767.

(154) Bluhm, H.; Andersson, K.; Araki, T.; Benzerara, K.; Brown, G. E.; Dynes, J. J.; Ghosal, S.; Gilles, M. K.; Hansen, H. C.; Hemminger, J. C.; Hitchcock, A. P.; Ketteler, G.; Kilcoyne, A. L. D.; Kneedler, E.; Lawrence, J. R.; Leppard, G. G.; Majzlan, J.; Mun, B. S.; Myneni, S. C. B.; Nilsson, A.; Ogasawara, H.; Ogletree, D. F.; Pecher, K.; Salmeron, M.; Shuh, D. K.; Tonner, B.; Tyliszczak, T.; Warwick, T.; Yoon, T. H. *J. Electron Spectrosc. Relat. Phenom.* **2006**, *150*, 86.

(155) Denecke, M. A.; Rothe, J.; Dardenne, K.; Blank, H. *Phys. Scr.* **2005**, *T115*, 1001.

(156) George, G. N. *EDG_FIT*; Stanford Synchrotron Radiation Laboratory: Stanford, CA.

(157) Becke, A. D. *J. Chem. Phys.* **1993**, *98*, 5648.

(158) Lee, C.; Yang, W.; Parr, R. G. *Phys. Rev. B* **1988**, *37*, 785.

(159) Frisch, M. J.; et al. *Gaussian 09, Revision B.01*; Gaussian, Inc.: Wallingford, CT, 2009.

(160) Fuentealba, P.; Preuss, H.; Stoll, H.; Vonszentpaly, L. *Chem. Phys. Lett.* **1982**, *89*, 418.

(161) Küchle, W.; Dolg, M.; Stoll, H.; Preuss, H. *Mol. Phys.* **1991**, *74*, 1245.

(162) Küchle, W.; Dolg, M.; Stoll, H.; Preuss, H. *J. Chem. Phys.* **1994**, *100*, 7535.

(163) Petersson, G. A.; Bennett, A.; Tensfeldt, T. G.; Al-Laham, M. A.; Shirley, W. A.; Mantzaris, J. *J. Chem. Phys.* **1988**, *89*, 2193.

(164) Petersson, G. A.; Al-Laham, M. A. *J. Chem. Phys.* **1991**, *94*, 6091.

(165) Shannon, R. D. *Acta Crystallogr.* **1976**, *A32*, 751.

(166) Cramer, C. J. *Essentials of Computational Chemistry*, 2nd ed.; Wiley: Chichester, UK, 2004.